Open access • Posted Content • DOI:10.1101/2021.09.30.462573

Structural Insights into the BRAF Monomer-to-dimer Transition Mediated by RAS Binding — Source link

Martinez Fiesco Ja, Durrant De, Deborah K. Morrison, Zhang P

Institutions: National Institutes of Health

Published on: 30 Sep 2021 - bioRxiv (Cold Spring Harbor Laboratory)

Topics: Binding domain

Structural Insights into the BRAF Monomer-to-dimer Transition Mediated by RAS Binding

Juliana A. Martinez Fiesco[1*], David E. Durrant[2*], Deborah K. Morrison[2^] and Ping Zhang[1^]

[1]Center for Structural Biology and [2]Laboratory of Cell and Developmental Signaling, Center for Cancer Research, National Cancer Institute-Frederick, Frederick, MD 21702

*** These authors contributed equally to this work**

^ *corresponding authors: morrisod@mail.nih.gov and ping.zhang@nih.gov

Summary

An unresolved issue in RAF kinase signaling is how binding of autoinhibited RAF monomers to activated RAS initiates the conformational changes required to form active RAF dimers. Here, we present cryo-electron microscopy structures of full-length BRAF complexes derived from mammalian cells: autoinhibited monomeric BRAF:14-3-3_2:MEK and BRAF:14-3-3_2 complexes and an inhibitor-bound, dimeric $BRAF_2$:14-3-3_2 complex, at 3.7, 4.1, and 3.9 Å resolution, respectively. The RAS binding domain (RBD) of BRAF is resolved in the autoinhibited structures, and we find that neither MEK nor ATP binding is required to stabilize the autoinhibited complexes. Notably, the RBD was found to interact extensively with the 14-3-3 protomer bound to the BRAF C-terminal site. Moreover, through structure-guided mutational studies, our findings indicate that RAS-RAF binding is a dynamic process and that RBD residues at the 14-3-3 interface have a dual function, first stabilizing RBD orientation in the autoinhibited state and then contributing to full RAS contact.

Introduction

The RAF kinases (ARAF, BRAF and CRAF/RAF1) are key intermediates in the RAS pathway, functioning as direct effectors of the RAS GTPases and as the initiating kinases in the ERK cascade, which is comprised of the RAF, MEK, and ERK protein kinases [1-3]. The RAS/RAF/MEK/ERK pathway plays a critical role in the transmission of signals that regulate cell proliferation, differentiation, and survival [4]. Signaling through this pathway is often dysregulated in cancer and the developmental RASopathy syndromes, and mutations in various components of the pathway, including the RAF kinases, can function as disease drivers [5-7].

Early analysis of the RAF kinases revealed the presence of three conserved regions CR1, CR2, and CR3 (reviewed in [2,3,8]). CR1 and CR2 are found in the N-terminal regulatory domain, with CR1 containing a RAS binding domain (RBD) and a cysteine-rich domain (CRD). CR2 is a region rich in serine/threonine residues and contains a phosphorylated 14-3-3 binding site (pS365 in BRAF). CR3 represents the C-terminal kinase domain and is followed by a second phosphorylated 14-3-3 binding site (pS729 in BRAF).

Over the years, biochemical studies have provided critical insights regarding the mechanisms that regulate RAF signal output. In quiescent cells, RAF kinases localize to the cytosol as inactive monomers [9], maintained in an autoinhibited state through intramolecular interactions between the RAF regulatory and catalytic domains together with the binding of a 14-3-3 dimer to the CR2 and C-terminal sites [10-13]. In response to signaling events and RAS activation, the RBD of RAF binds directly to GTP-bound RAS at the plasma membrane [14-17], resulting in the disruption of the autoinhibited conformation, dimerization of RAF kinase domains, and catalytic activation through an allosteric mechanism [18-21]. Once activated, RAF can then initiate the phosphorylation cascade, which leads to the sequential activation of MEK and ERK [22].

Using X-ray crystallography or NMR spectroscopy, numerous structures of dimerized RAF kinase domains and other isolated regions of RAF have been solved; however, the structural determination of full-length monomeric and dimeric RAF complexes has been challenging due to the number of proteins that associate with RAF as well as the largely unstructured nature of the N-

terminal regulatory domain. Nevertheless, recent cryo-electron microscopy (cryo-EM) and crystal structures of BRAF have shed light on these complexes, providing visual context to the knowledge obtained through biochemical and cell biological approaches [13,23,24]. For example, the published cryo-EM structure of an autoinhibited, monomeric BRAF complex confirmed that a 14-3-3 dimer can bind simultaneously to the BRAF pS365 and pS729 sites and that the CRD makes critical contacts with both the RAF catalytic domain and the 14-3-3 dimer in the autoinhibited state [13], consistent with previous studies implicating the CRD and 14-3-3 as key regulators of RAF autoinhibition [10,12,25,26]. Binding of the 14-3-3 dimer was also found to occlude both the membrane/ligand binding region of the CRD and the dimer interface of the kinase domain [13], thus preventing spurious CRD-membrane contact as well as RAF dimer formation. In contrast, the RBD was not sufficiently resolved in the autoinhibited complex to determine its exact position or orientation [13]. As a result, questions regarding whether the RBD interacts with other BRAF domains or the 14-3-3 dimer in the autoinhibited state remained open. Moreover, no insight was gained regarding how RAS binding relieves RAF autoinhibition and promotes the conformational changes needed for dimerization and kinase activation. In addition, recent BRAF dimer structures have shown that the 14-3-3 dimer can bind simultaneously to two kinase domain protomers, but whether both protomers are catalytically active has been a matter of debate [13,23,24,27].

Using a mammalian cell expression system to isolate BRAF complexes, here we report the cryo-EM structures of two autoinhibited, monomeric BRAF complexes in which the RBD is well-defined. Only one of the autoinhibited complexes included MEK, but both contained a bound 14-3-3 dimer, and in both structures, the kinase domain was in a canonical inactive configuration and lacked ATP. In addition, we also report the cryo-EM structure of a BRAF dimer complex with both BRAF protomers bound to an ATP-competitive BRAF inhibitor and the kinase domain assuming an active conformation. The dimeric BRAF complex also included a dimer of 14-3-3 that bridged the C-terminal pS729 sites on each BRAF protomer, and the dimerized kinase domains exhibited an asymmetric orientation with respect to the 14-3-3 dimer. Notably, resolution of the RBD in our autoinhibited, monomeric BRAF structures provides key insights regarding how

the orientation of the RBD allows access for RAS binding and how the interaction with RAS facilitates the the monomer-to-dimer transition required for RAF activation.

Results

Isolation and Initial Characterization of BRAF Complexes

To isolate BRAF complexes for cryo-EM analysis that would accurately reflect the regulatory mechanisms that take place in mammalian cells, we first established a human 293 FT cell line that stably expressed full-length, wild-type (WT) BRAF containing an N-terminal Halo tag (Figure 1A). Using this cell line, monomeric BRAF complexes were isolated from quiescent, serum-depleted cells. Dimeric BRAF complexes were also isolated using cycling cells that were treated with the BRAF inhibitor SB590885 for 18 hours to promote RAF dimerization. BRAF complexes were collected from cell lysates using affinity chromatography and then separated by gel filtration chromatography to obtain homogenous samples containing recombinant BRAF in association with various endogenous proteins (Figures S1A-C). Analysis of the gel filtration fractions obtained from serum-depleted cells indicated a well-defined peak of monomeric BRAF that was comprised of two distinct physiological complexes, a larger complex containing 14-3-3 proteins and MEK (fraction 18) and a smaller complex containing 14-3-3 proteins but lacking MEK (fraction 19) (Figure S1A). To maximize purity and homogeneity of the MEK-bound complex, an additional protein preparation was generated from serum-depleted cells that had been treated with the MEK inhibitor CH5126766 to stabilize the BRAF-MEK interaction (Figure S1B). Analysis of the gel filtration fractions obtained from the RAF inhibitor SB590885-treated cells indicated a prominent peak near fraction 16 that represented a larger complex containing primarily BRAF and 14-3-3 proteins, with MEK and Hsp70 also observed (Figure S1C).

Mass spectrometry analysis of each of the three sample complexes revealed that 14-3-3ε and 14-3-3ζ constituted approximately 50% and 25%, respectively of the 14-3-3 proteins present in both the monomeric and dimeric BRAF complexes (Figure S1D). However, all other 14-3-3 isoforms were detected, consistent with the propensity of 14-3-3 proteins to heterodimerize with

other family members. For the MEK-bound monomeric BRAF complex, MEK1 and MEK2 were present at a 54% and 46% ratio, respectively (Figure S1D). It should be noted that for the structures derived from cryo-EM, we used the human 14-3-3ζ isoform (PDB ID: 4FJ3) as a starting model for the 14-3-3 dimer and MEK1 (PBD ID: 3WGI) to represent MEK in the MEK-bound, autoinhibited complex.

Structural analysis of the inhibitor-bound dimeric $BRAF_2$:14-3-3_2 complex

A major advance in understanding RAF activation originates from studies showing that under most signaling conditions, dimerization of the kinase domains is required [28]. Many structures of isolated, dimeric BRAF kinase domains have been solved; however, recent structures of BRAF dimer complexes containing 14-3-3 proteins [13,23,27] have raised new questions regarding the mechanisms of dimer activation and whether both protomers in the dimer have catalytic activity. To further investigate these issues, we isolated BRAF dimer complexes from mammalian cells treated with the ATP-competitive BRAF inhibitor SB590885 and obtained a cryo-EM structure of full-length, inhibitor-bound $BRAF_2$:14-3-3_2 at 3.9Å resolution (Figure 1B-C, S2A-C). It should be noted that despite the presence of MEK in the cryo-EM sample fraction, no density corresponding to MEK was observed in the 3D reconstructions. Additionally, the RBD and CRD as well as other regions of the N-terminal regulatory domain (residues 1-448) were also missing from the density map and are expected to be solvent exposed and flexible. In our inhibitor-bound $BRAF_2$:14-3-3_2 structure, the BRAF kinase domains (KD) adopt a canonical back-to-back orientation with the αC-helices in the active "in" position and the regulatory (R) spines aligned [21,29] (Figure 1 B-C, S2D-E). As expected, a 14-3-3 dimer was bound to each C-terminal pS729 site, forming a stabilizing bridge between the KD protomers.

The orientation of the KD dimer with respect to the 14-3-3 dimer was asymmetric and similar to that previously described for a cryo-EM structure of a ligand-free $BRAF_2$:14-3-3_2 complex [23] (Figure 1C), with our structure superimposing well onto the ligand-free dimer structure, with an overall Cα root mean square deviation (RMSD) of 1.03 Å. Notably, a major difference

between the two structures is that for the unliganded $BRAF_2$:14-3-3_2 structure, the distal C-tail segment (F743 to A749) of one KD protomer was found to insert into the active site of the other protomer, thus inhibiting its catalytic activity. Moreover, insertion of the C-tail segment into the active site was proposed to allow the "inhibited" protomer to act as a transactivator of the promoter from which the C-tail emanated and was also thought to account for the asymmetric orientation of the KD and 14-3-3 dimers.

In our inhibitor-bound $BRAF_2$:14-3-3_2 structure, interpretable density for both C-tails stops at residue 733, indicating that the C-tails (residues 734 to 766) are flexible after exiting the 14-3-3 binding pocket (Figure 1B-C). In addition, density corresponding to the RAF inhibitor SB590885 was observed in both active sites (Figure 1B-C, S2D) and overlapped with the position of the C-tail segment in the ligand-free dimer structure (Figure 1C). This finding shows that insertion of the C-tail into the active site can be overcome by inhibitor binding and is consistent with recent biochemical analyses of active $BRAF_2$:14-3-3_2 complexes using differential scanning fluorimetry, microscale thermophoresis, and surface plasmon resonance approaches, which indicated that both ATP binding sites are available for ligand binding even when the C-tail segment is present [24]. Our inhibitor (SB590885)-bound $BRAF_2$:14-3-3_2 structure was also found to overlap well with the high resolution crystal structure of inhibitor (GDC-0879)-bound BRAF KD (residues D432–R735)$_2$:14-3-3_2 complexes [27] (Cα RMSD of 0.80 Å). In this structure, GDC-0879 was found in the active sites of both protomers, and even though the KDs lacked the C-tail segments, an asymmetric orientation between the BRAF KD and the 14-3-3 dimer was observed. Taken together, our findings add support to the model that the asymmetry between the KD and 14-3-3 dimers is not determined by C-tail insertion and that the active sites of both protomers may bind ATP simultaneously to promote catalysis.

Structural analysis of the monomeric BRAF:14-3-3_2:MEK and BRAF:14-3-3_2 complexes

Over the years, less has been known regarding the structure of autoinhibited RAF monomers, with only one cryo-EM structure reported for full-length monomeric BRAF [13]. Here, using serum-

depleted mammalian cells, we were able to isolate two monomeric BRAF complexes of sufficient homogeneity for structural analysis using cryo-EM, resulting in a BRAF:14-3-3_2:MEK structure of 3.7 Å resolution and a BRAF:14-3-3_2 structure of 4.1 Å resolution (Figure 2A, S3A-C). Strikingly, except for the presence or absence of MEK, the overall conformation of the monomeric BRAF structures was nearly identical, with an overall Cα RMSD of 0.95 Å for the corresponding BRAF:14-3-3_2 portions and an RMSD of 0.99 Å for the BRAF KDs. In these structures, the BRAF monomer exhibits an autoinhibited conformation with a 14-3-3 dimer bound to the canonical pS365 and pS729 sites and the CRD making stabilizing contacts with the C-lobe of the kinase domain and with both protomers of the 14-3-3 dimer (Figure 2A, S3D). These results are consistent with the previously determined BRAF:14-3-3_2:MEK1^{S218A,S222A} structure [13]; however, they demonstrate that MEK binding is not required for BRAF to assume a stable, autoinhibited conformation.

The BRAF kinase domain in both our monomer structures displayed the canonical kinase inactive conformation [21,30], with the αC-helix in the "out" position and the R-spine broken (Figure 2A and S4A). Residues in the activation segment (residues 598-602) formed an inhibitory turn to reinforce the extended outward shift of the αC-helix (Figure S4A). Although the ATP binding pocket was unoccupied in our monomer structures, the structure of the KDs displayed an almost identical conformation as did recent inactive KD structures bound to ATP analogs, namely the ATP-γ-S-bound BRAF:14-3-3_2:MEK1^{S218A,S222A} structure; Cα RMSD of 0.90 Å [13] and the BRAF KD (AMP-PCP):MEK1 structure (KD Cα RMSD of 0.82 Å) [24] (Figure S4B-C). Moreover, as was reported for the ATP-analog-bound structures, the N- and C-lobes of the KD in our ATP-free structure exhibited a closer orientation than is observed for the lobes of KDs bound to RAF inhibitors (Figure S4B) [13,24,31,32]. These findings indicate that the ATP binding pocket of the BRAF KD is stable in the "apo" nucleotide-free state and that the compact configuration of the N- and C-lobes as well as the autoinhibited BRAF conformation are not dependent on ATP binding (Figure S4B-C).

For the larger monomeric BRAF complex containing MEK, the active sites of MEK and the BRAF KD are in a canonical face-to-face orientation, with the C-lobes of both kinases making extensive contacts and the activation segments running in an antiparallel manner (Figure 2A and S4D). As expected, MEK was in the inactive conformation with its αC-helix in the "out" position and density for the MEK inhibitor CH5126766 visible within the allosteric binding site (Figure S4D). In addition, residues of the αA-helix of MEK, which acts in a negative regulatory manner to stabilize the inactive conformation [33], were resolved and lay against the base of the MEK αC-helix (Figure S4D).

Consistent with the previously published autoinhibited BRAF:14-3-3$_2$:MEK1^{S218A,S222A} structure, the N-terminal segment of BRAF (amino acids 1-155) and the linker sequences between the CRD and the pS365 site (amino acids 281-359), and between the pS365 site and the kinase domain (amino acids 371-448) are not resolved in our monomeric structures, likely reflecting the flexibility of these regions. In contrast, the RBD is well-defined in both our autoinhibited BRAF:14-3-3$_2$:MEK and BRAF:14-3-3$_2$ structures, revealing the position and orientation of this critical domain (Figure 2A and S3D).

RBD Orientation and Contacts in the Autoinhibited Monomeric BRAF Complexes

A distinct feature of the BRAF structures reported here is the resolution of the RBD in the context of the full-length, autoinhibited BRAF monomer. RBDs are known to have a conserved ubiquitin-like structure [34] containing five beta strands and two to three alpha helices. As shown in Figure 2A, the BRAF RBD in both the monomeric structures sits on top of the 14-3-3 protomer bound to the C-terminal pS729 site and adjacent to the C-lobe of the KD, with N163 of the RBD being within hydrogen bond distance to S679 of the KD (Figure S4E). No RBD contact is observed with the CRD or MEK, in the MEK-bound structure. Notably, an extensive contact surface of ~435 Å^2 is observed between the RBD and the 14-3-3 protomer, with the electrostatic charge distributions of the interface surfaces having considerable complementarity (Figure 2B). The α1-helix of the RBD is oriented along the interface and interacts extensively with the α8-helix, α9-helix, and loop

8 of 14-3-3 (Figure 2B-C). The 14-3-3 residues involved in this interface are conserved in all human 14-3-3 family members, indicating that a similar interface would be predicted regardless of the isoform composition of the 14-3-3 dimer. In contrast, two RBD residues at the center of the RBD:14-3-3 interface, M186 and M187, are not conserved, being replaced by a lysine and valine in CRAF and ARAF (Figure 2C).

Because the M186 and M187 residues have the potential to make numerous contacts with 14-3-3 at the interface and given that contacts between 14-3-3 and the CRD are known to play a key role in maintaining the autoinhibited state, we next took a mutational approach to determine whether these RBD residues also contribute to RAF autoinhibition. M186 and M187 were mutated either to lysine and valine (as in CRAF and ARAF), to tryptophanes, which are bulkier residues but still hydrophobic, or to smaller alanine residues, following which the effect of these mutations on RAF autoinhibition was assessed using a proximity-based NanoBRET assay. In this assay, BRAF is split into two segments, with the regulatory domain (1-435) tagged with an acceptor fluorophore ($BRAF^{REG}$-Halo Tag) and the kinase domain (436-766) tagged with an energy donor (NanoLuc- $BRAF^{KD}$). When the two segments interact to form an autoinhibited complex that is stabilized by 14-3-3 dimer binding, the donor and acceptor are brought within range for energy transfer to occur (<100 Å), resulting in the generation of a BRET signal. As a control, we found that when the CRD of $BRAF^{REG}$ contained the RASopathy-associated T241P mutation, which reduces the autoinhibitory effect of the CRD, the BRET signal was decreased approximately 50%. Analysis of the RBD mutants reavealed that the M186K/M187V mutant generated a BRET signal that was equivalent to WT-$BRAF^{REG}$. In contrast, a reproducible 10% decrease in signal was observed for the M186W/M187W mutant, whereas a 20% increase in signal was observed for the M186A/M187A mutant. M186A/M187A-$BRAF^{REG}$ was also found to be more effective at suppressing MEK activation mediated by the isolated $BRAF^{KD}$ protein than was WT-$BRAF^{REG}$ (Figure 2D), indicating an enhanced ability to form a stable, autoinhibited BRAF complex (Figure 2E). In addition, when incorporated into full-length BRAF, the M186W/M187W exhibited an increased biological activity in focus forming assays (Figure 2F). Moreover, the activity of the

RBD M186W/M187W and CRD T241P mutants in the focu forming assay correlated with the ability of these mutations to disrupt RAF autoinhibition in the BRET assay. Thus, while the CRD plays a predomiant role in auoinhibition, these findings indicate that M186/M187 and the RBD also contribute to the maintenance of the autoinhibited state.

Effects of RAS Binding on the BRAF RBD:14-3-3 Interface

Under normal signaling conditions, the RAF activation process begins when an autoinhibited RAF monomer interacts with GTP-bound RAS [14-16]. The initial contact with RAS is made by the RAF RBD, whereby the β2-strand and the α1-helix of the RBD interacts with the β2-strand and the switch I region of RAS [35,36]. RAS-RBD binding involves ionic and hydrogen bonds as well as other non-bonded interactions [37]. In our autoinhibited BRAF complexes, the RAS binding surface of the RBD faces away from the CRD and is oriented towards a space that we term the "RAS pocket" (Figure 3A). This pocket is flanked by 14-3-3, the C-lobe of the KD, and MEK in the BRAF:14-3-3_2:MEK structure (Figure 3A-B). Critical basic residues of the RBD, R158, R166, K183 and R188, are exposed and face towards the RAS pocket, ready to form ionic bonds with acidic residues E31, D33, E37 and D38 in RAS switch I (Figure 3B).

To demonstrate that the RBD in our autoinhibited BRAF monomeric complexes is accessible for RAS binding, fluorescence polarization assays were conducted in which the purified BRAF:14-3-3_2:MEK and BRAF:14-3-3_2 complexes were titrated onto GFP-KRAS that had been pre-loaded with a GTP analog. As shown in Figure 3C, both complexes exhibited a high degree of binding and had affinities in the nanomolar range. RAS-RAF binding could also be demonstrated in $KRAS^{G12V}$ pull-down assays using the purified BRAF:14-3-3_2:MEK and BRAF:14-3-3_2 complexes (Figure 3D). As expected, individual mutation of each of the four RBD basic residues that form ionic bonds with KRAS, R158A, R166A, K183, and R188L, significantly disrupted $KRAS^{G12V}$ binding in the pull-down assays (Figure 3E), confirming that RBD contact is essential for the RAS-BRAF interaction.

Although it has been known that binding to RAS relieves RAF autoinhibition and allows RAF to dimerize, the precise molecular details for how this is achieved has been unclear. Based on the known KRAS:RBD interface [37], we superimposed KRAS onto our autoinhibited BRAF structures such that all interactions needed for high affinity binding could form. Strikingly, in this position, a steric clash would occur between residues in the KRAS α1-helix and switch I region and the α8- and α9- helices of 14-3-3 that lie beneath the RBD and form the interface region with the RBD (Figure 3F). Specifically, RAS residues I21, Q22 (α1-helix), Q25-E31 (SI region), K42 and V45 (β2 sheet) would clash with 14-3-3 α8-helix residues C189, A192-E198, I200, A201 and α9-helix residues R222, L225, T226 and S230 (Figure S4F). Moreover, this region of 14-3-3 has a notable negative charge and, while complementary with the positively charged RBD interface, would cause electrostatic repulsion with negatively charged residues in KRAS switch I (Figure 3F). In particular, KRAS switch I residues D30 and E31 would be brought in close proximity to D197 and E198 of 14-3-3.

The above findings indicate that a conformational change in 14-3-3 binding must occur in order for RAS to establish full contact with the BRAF RBD. Thus, we propose a model whereby binding between RAS and BRAF is a dynamic process in which the autoinhibited BRAF monomer is first recruited to the membrane through initial contact between RAS and the RBD, likely mediated through ionic interactions with exposed basic residues of the RBD. This initial interaction would generate steric clashes and electrostatic repulsion between RAS and 14-3-3 at the RBD:14-3-3 interface that would facilitate the rearrangement of 14-3-3 dimer binding and expose additional RBD residues predicted to be involved in full RAS-RBD contact. The full spectrum of RAS-RBD interactions would dislodge the RBD and in turn the CRD from the autoinhibited complex, thereby enabling the CRD to rotate and make contact with RAS and the plasma membrane. This structural rearrangement, in turn, would expose the BRAF dimer interface to allow for dimer formation and catalytic activation.

In support of this model, our results indicate that the RBD M186/M187 residues at the center of RBD:14-3-3 interface serve a dual role by mediating contact with 14-3-3 in the autoinhibited state and by contributing to RAS binding interactions upon RAS activation. These methionines are a lysine and valine in CRAF, and structural studies indicate that K87 and V88 of CRAF contributes to full RAS:RBD contact by forming extenstive non-electrostatic interactions with KRAS residues I24, Q25, and Y40 [37]. Although M186 and M187 in BRAF are partially or fully occulded by 14-3-3 in the autoinhibited state, the steric clash cause by initial RAS:RBD contact would directly impact 14-3-3 residues that interact with these methionines, perhaps resulting in their exposure for interactions with RAS. Therefore, to address whether these BRAF residues contribute to the RAS-RBD interaction, the M186/M187 mutants were assessed for binding to $KRAS^{G12V}$ in co-immunoprecipitation experiments and in a BRET assay that monitors RAS-RAF binding in live cells. In particular, by conducting saturation curves, the BRET assay allows for the level of RAS-RAF binding ($BRET_{max}$) to be quantified as well as the affinity of the interaction ($BRET_{50}$) [38]. Intriguingly, when both the M186/M187 residues were mutated to alanine, reduced binding to $KRAS^{G12V}$ was observed in the coimmunoprecipitation assays (Figure 4A) and a reduction in both the levels and affinity of $KRAS^{G12V}$ binding was observed in the BRET assays (Figure 4B). In contrast, when M186/M187 were mutated to bulkier tryptophan residues (M186W/M187W) or changed to lysine and valine (M186K/M187V), as in CRAF, increased levels of binding to KRAS were observed in both the BRET and coimmunoprecipitation assays (Figure 4A-B).

To test whether the modulation in binding reflects direct RAS-RBD contact, RBD pulldown experiments were performed using isolated WT or mutant BRAF RBD domains. As was observed for the full-length BRAF proteins, the M186A/M187A mutant exhibited reduced RBD binding to $KRAS^{G12V}$, whereas the M186W/M197W and the M186K/M187V mutants exhibited increased binding (Figure 4C), indicating that the mutations were directly influencing interactions between the BRAF RBD and $KRAS^{G12V}$. Modeling of the amino acid substitutions

(Figure 4D) into the K87/V88 positions of a CRAF RBD:RAS structure [37] further supports these findings in that while the KV/MM substitutions would change some of the backbone and side chain interactions, non-eletrostatic interactions would still be predicted. With the KV/WW mutations, the bulkier tryptophan residues would have the potential to form additional interactions, whereas the alanine substitutions would results in the loss of all side chain contacts. Thus, taken together our mutational analysis indicates that these central residues in the BRAF RBD:14-3-3 interface serve dual functions in first contributing to the autoinhibited state through interactions with 14-3-3 and then in contributing to the full spectrum of RAS-RBD interactions that facilitates the conformation changes needed to disrupt the autoinhibited state.

Discussion

It is well established that under most signaling conditions binding to activated RAS is required for RAF dimerization and activation; however, the structural details for how RAS binding allows autoinhibited RAF monomers to assume an activate dimer conformation has been unclear. In this study, we successfully obtained cryo-EM structures of autoinhibited, monomeric BRAF complexes (BRAF:14-3-3_2:MEK and BRAF:14-3-3_2 at 3.7 and 4.1 Å resolution respectively) and a RAF inhibitor-bound dimeric complex ($BRAF_2$:14-3-3_2 at 3.9 Å resolution). These complexes were isolated from a mammalian cell expression system such that components of the complex would be subject to normal cellular regulation and more closely represent authentic signaling complexes. The autoinhibited BRAF structures show that prior to signaling events, BRAF and its substrate MEK can exist as a preassembled BRAF:14-3-3_2:MEK complex; however, the interaction with MEK is not required for BRAF to assume a stable autoinhibited conformation. Similarly, our structures show that the ATP-binding site is fully formed in the "apo" state and that stabilization of the autoinhibited state is also not dependent on ATP binding. Notably, both our autoinhibited BRAF monomeric structures had clearly resolved RBDs, revealing the position and

orientation of this critical domain and providing valuable insight regarding how RAS binding facilitates the monomer to dimer transition.

The position and orientation of the RBD in the context of the autoinhibited BRAF complexes indicates that the RBD is accessible for RAS binding, with key basic residues involved in RAS contact exposed. However, it should be noted that the large BRAF specific, N-terminal segment that precedes the BRAF RBD was not resolved in our structures. Thus, it is possible that this region, may represent addition levels of regulation in terms of the RAS-BRAF interaction, as has been suggested in recent live cell studies analyzing the binding preferences of the RAS and RAF family members [38]. Nonetheless, both the purified BRAF:14-3-3$_2$:MEK and BRAF:14-3-3$_2$ complexes were fully competent to bind GTP-bound KRAS in fluorescence polarization assays and displayed high affinity binding. Our autoinhibited structures also revealed a significant contact interface between the RBD and the 14-3-3 protomer bound to the C-terminal pS729 site. The interface surfaces had charge complementarity, with the RBD surface containing several positively charged residues and the 14-3-3 surface having a predominant negative charge. The 14-3-3 residues that comprise the interaction surface are conserved in all 14-3-3 family members, indicating that the surface would be the same irrespective of which isoform was bound.

Strikingly, our results indicate that two RBD residues at the center of RBD:14-3-3 interface, M186/M187, also contribute to RAS binding and may play a key role in facilitating the conformational changes in 14-3-3 binding that are needed for dimer formation. Recent crystal structures analyzing CRAF RBD and CRAF RBD-CRD binding to KRAS indicates that residues in the analogous position in the CRAF RBD (K87/V88) make non-bonded interactions with three RAS residues, I24/Q25/Y40 [37], and while there is no structure of RAS bound to the BRAF RBD, our mutational analysis of the BRAF RBD M186/M187 residues suggests that alterations in these residues can modulate KRAS binding. Thus, integrating our autoinhibited BRAF structures into what is known regarding the RAS-RBD interaction strongly supports a model whereby RAS binding is a highly dynamic process (Figure 5). The initial contact with activated RAS is likely made by exposed basic residues in the BRAF RBD (R158, R166, K183, R188). As RAS is

engaged to form the high affinity ionic bonds, a steric clash and electrostatic repulsion between RAS and 14-3-3 would occur at the RBD:14-3-3 interface, leading to the exposure of additional RBD residues involved in the full spectrum of RAS-RBD interactions. We predict that together these events will dislodge the RBD and in turn the CRD from the autoinhibited structure, thus putting further strain on the bound 14-3-3 dimer that ultimately results in its release from the pS365 site. The freed CRD could then contact RAS and the plasma membrane to further stabilize RAS-RAF complexes and aid in orienting the KD for dimer formation. It should be noted that crystal structures of RAS bound to a truncated CRAF protein containing only the RBD-CRD have recently been reported (HRAS:CRAF_RBD-CRD [39] and KRAS:CRAF_RBD-CRD complexes [37]) and demonstrate significant contact of the CRAF CRD with RAS. Based on the position and orientation of the RBD and CRD in our autoinhibited BRAF structures, it appears that if the BRAF CRD makes similar contacts with activated RAS, the CRD would need to rotate as it is dislodged from autoinhibited complex in order to assume the final RAS binding state. More specifically, when the bound RBD-CRD structure is overlayed onto our autoinhibited structure, with the alignment based on the CRD position, the RBD of the CRAF_RBD-CRD structure would lie outside the cryo-EM density map (Figure S4G). Thus, the RAS:CRAF_RBD-CRD structure may be more representative of the final RAS-BRAF binding conformation rather than the initial contact between RAS and the autoinhibited BRAF complexes. Alternatively, the structures of autoinhibited BRAF and CRAF complexes may vary and/or the contacts between RAS and the RBD-CRD regions of BRAF and CRAF may be different.

Not surprising, given the critical role of the membrane environment in forming the active dimeric RAF complex, the entire regulatory region of BRAF was unstructured in our dimeric $BRAF_2$:14-3-3_2 complex. As RAF inhibitor treatment was used to facilitate the isolation of dimer complexes, SB590885 was detected in the ATP-binding pocket of both KD protomers. Each KD protomer also interacted with a protomer of a 14-3-3 dimer, which was bound to the C-terminal pS729 site. The orientation between the KD and 14-3-3 dimers was asymmetric and similar to that observed in the other structures of dimerized BRAF KDs bound to 14-3-3 [23,24,27]. This

asymmetry was initially proposed to result from the insertion of a C-tail segment from one BRAF KD protomer into the active site of the other [23]; however, the fact that a similar orientation has been observed when the active sites are fully occupied by RAF inhibitors or when the KDs lack the C-terminal segments has argued against this model [24,27].

Finally, comparison of the KD conformation in our inhibitor-bound BRAF dimer complexes with that of the autoinhibited, monomeric BRAF structures is in agreement with previous observations that the N- and C-lobes of the inhibitor-bound dimerized complexes are in a more open configuration [13,27]. Interestingly, in our monomeric BRAF structures, this compact kinase domain configuration, which is known to put the dimer interface in an unfavorable position to form the N- to C-lobe antiparallel interactions needed to form dimers, was observed in the absence of ATP binding, differing from the previously reported structures exhibiting this conformation [13,27]. Nonetheless, our findings are in agreement with the model that identifying compounds or strategies to stabilize this compact configuration may have therapeutic potential in blocking aberrant RAF dimerization.

In summary, our studies contribute to the understanding of the BRAF signaling process by providing biochemical and structural information regarding different BRAF states. Further investigation is still needed to tease out the mechanistic details for the transition between states and how these transitions are altered by events such as phosphorylation, dephosphorylation, changes in the signaling environment, and interactions with other binding partners. Moreover, it will be important to determine if other RAF family members have similar monomer and dimer architectures and whether heterodimer complexes may differ. This knowledge will provide a more mechanistic understanding of the signaling process and may aid in the development of more effective treatment strategies for RAS- and/or RAF-driven disease states.

Acknowledgements

This research was supported by Federal funds from the National Cancer Institute, National Institutes of Health, under project numbers ZIA BC 010329 (D.K.M) and ZIA BC 011744 (P.Z.).

This work utilized the NCI/NICE cryo-EM Facility, and we would like to thank Dr. Rick Huang for help with cryo-EM data collection. The authors also thank Dr. Dan Shi and Dr. Dewight Williams for their assistance in collecting diagnostic cryo-EM data at the NCI-Frederick cryo-EM Facility and at the John M. Cowley Center for High Resolution Electron Microscopy, Arizona State University, respectively and for their helpful discussions. In addition, we thank Dr. Ming Zhou (Inova Schar Cancer Institute) for mass spectrometry analysis of the BRAF complexes, Elizabeth Terrell for technical assistance in performing the RAS/RAF BRET assays, and Dr. Dominc Esposito (FNLCR Protein Expression Laboratory) for the KRAS protein used in fluorescent polarization assays. This study utilized the computational resources of the High-Performance Computing Biowulf cluster of the NIH (http://hpc.nih.gov).

Author Contributions

J.A.M.F., D.E.D., D.K.M., P.Z. conceived the project, interpreted the results, and wrote the paper. D.E.D. expressed and affinity purified all BRAF complexes. J.A.M.F. further purified all BRAF complexes by size exclusion chromatography and performed fluorescence polarization assays. D.E.D. performed mutagenesis, co-immunoprecipitation, pull-down, and BRET assays. J.A.M.F. screen, optimized, prepare cryo-grid samples, and collected electron microscopy data. J.A.M.F. and P.Z. processed, built, and analyzed Cryo-EM models. D.K.M. and P.Z. provided funding resources and supervision.

Declaration of Interests

The authors declare no competing interests.

Figures

Figure 1

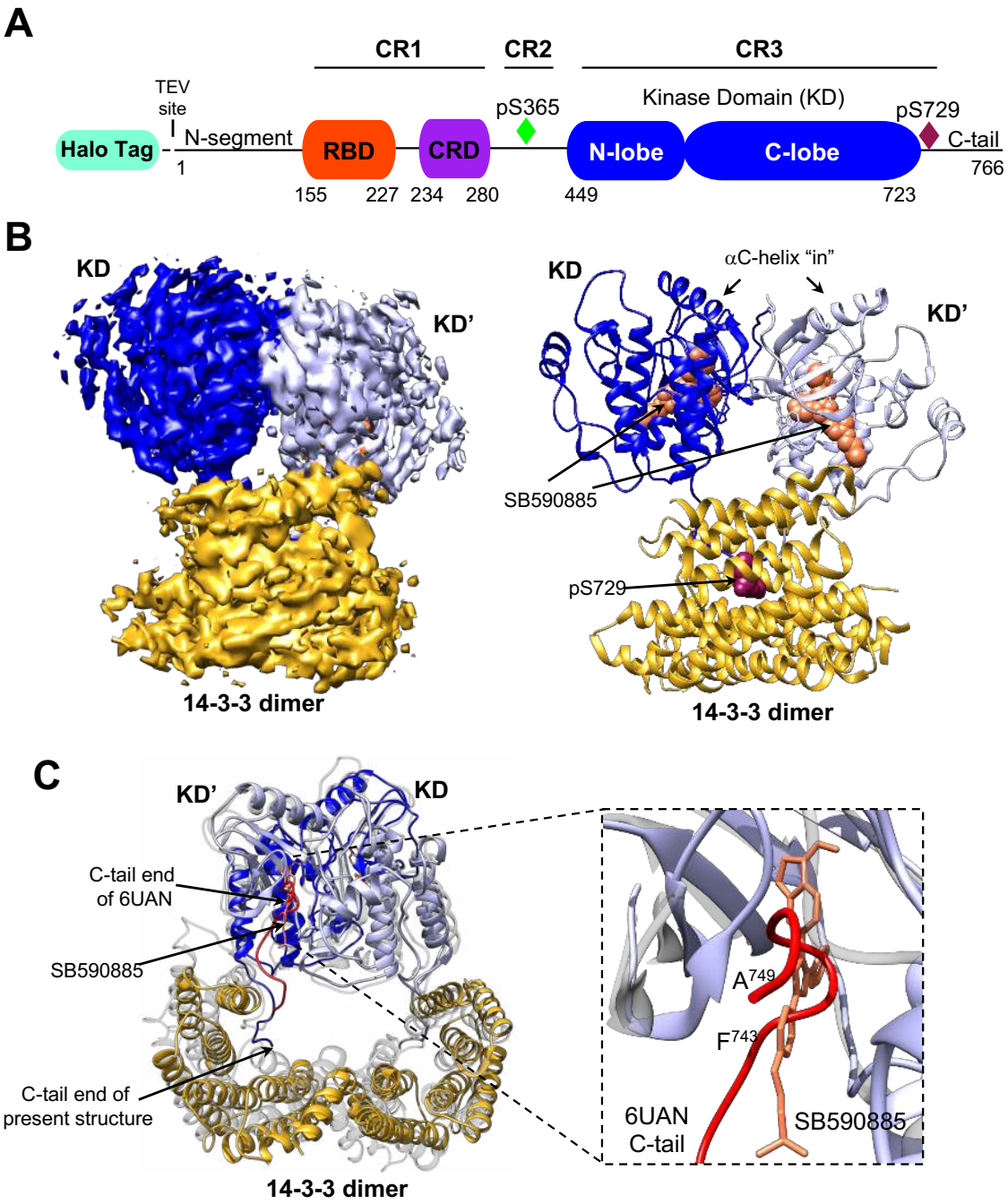

Figure 2

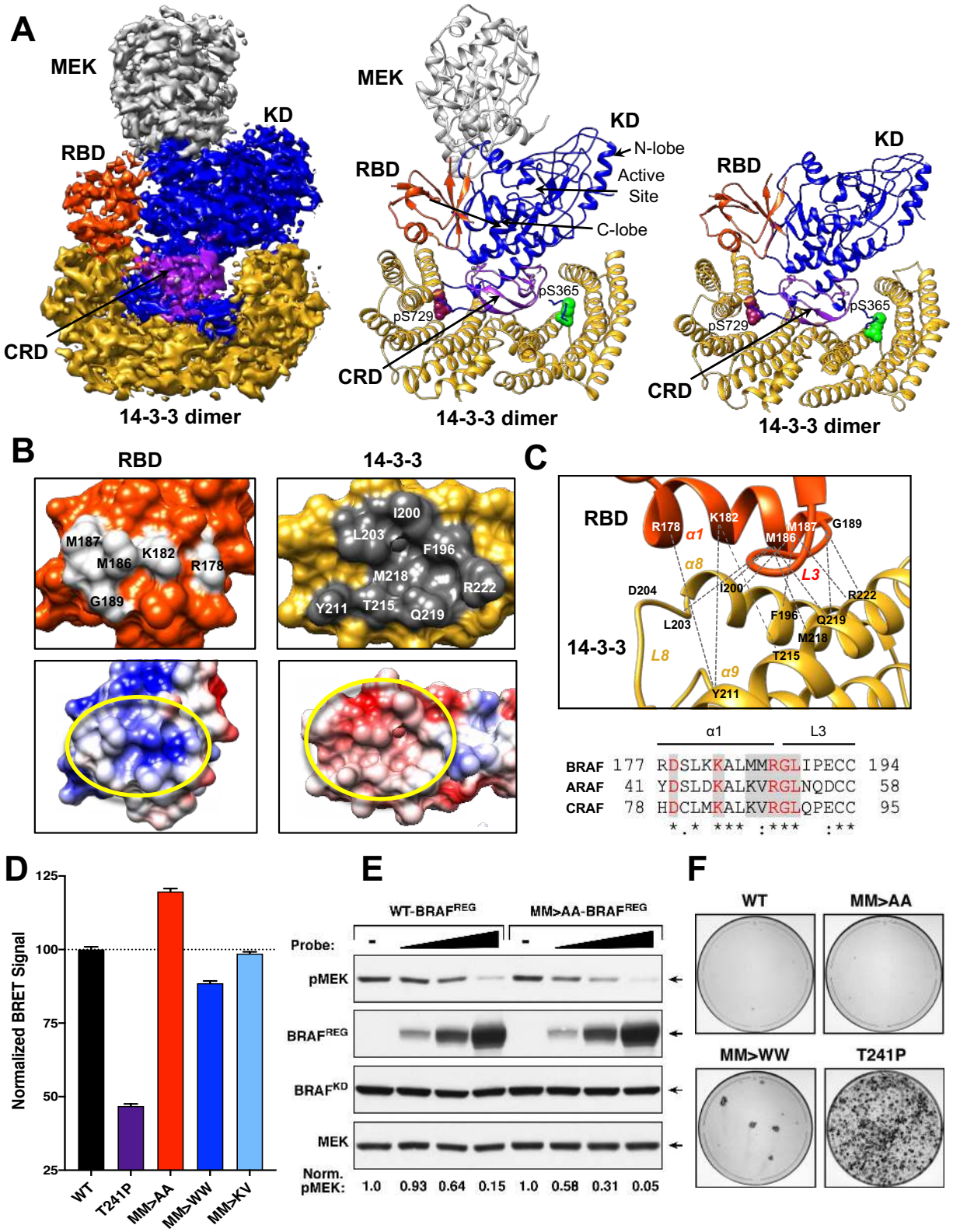
A
MEK
KD
RBD
CRD
14-3-3 dimer
N-lobe
Active Site
C-lobe
pS365
pS729
B
RBD
14-3-3
M187
K182
M186
R178
G189
I200
L203
F196
M218
R222
Y211
T215
Q219
C
α1
L3
α8
α9
L8
D204
BRAF 177 RDSLKKALMMRGLIPECC 194
ARAF 41 YDSLDKALKVRGLNQDCC 58
CRAF 78 HDCLMKALKVRGLQPECC 95
D
Normalized BRET Signal
125
100
75
50
25
WT
T241P
MM>AA
MM>WW
MM>KV
E
WT-BRAF^REG
MM>AA-BRAF^REG
Probe:
pMEK
BRAF^REG
BRAF^KD
MEK
Norm. pMEK:
1.0 0.93 0.64 0.15 1.0 0.58 0.31 0.05
F
WT
MM>AA
MM>WW
T241P

Figure 3

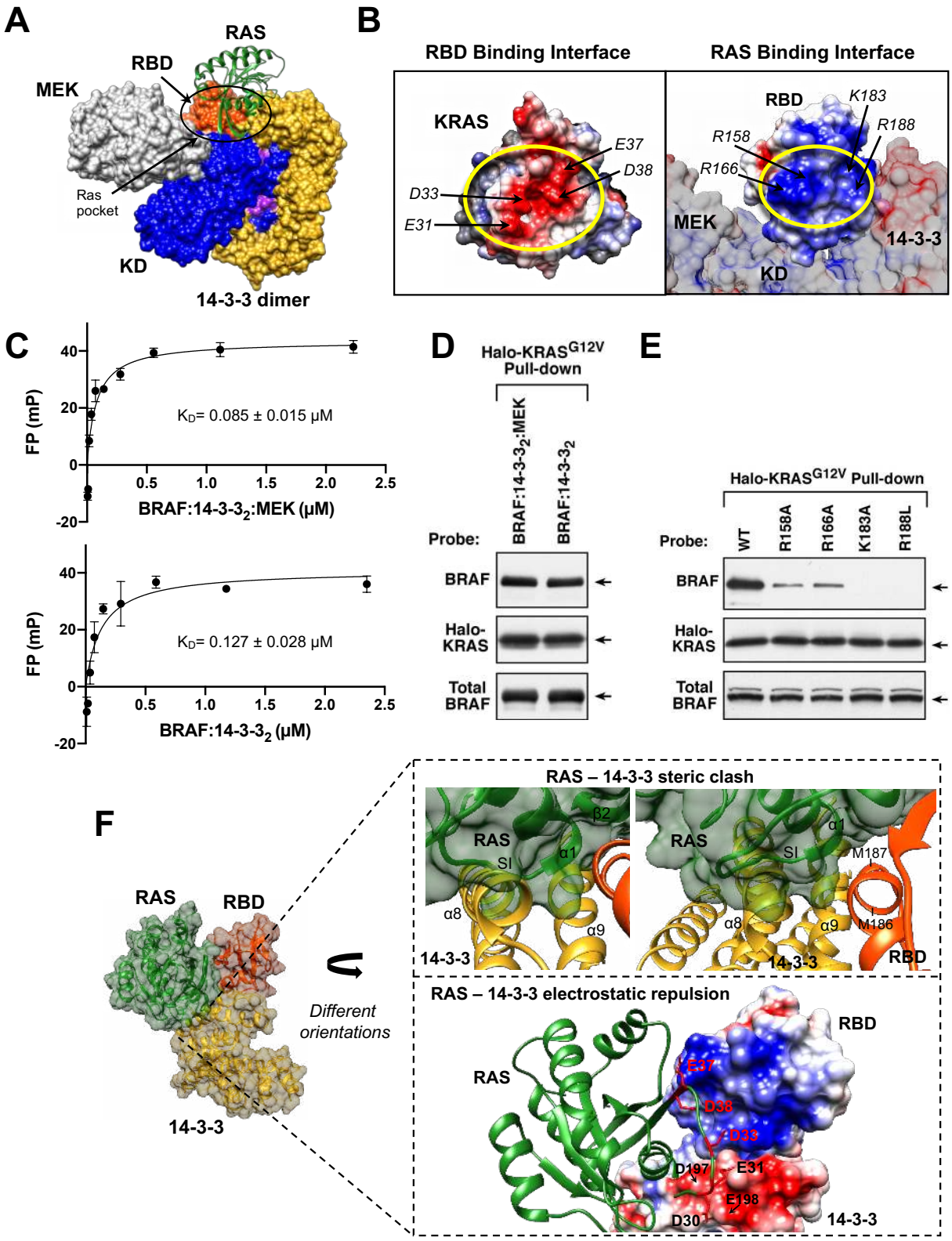
A
RAS
RBD
MEK
Ras pocket
KD
14-3-3 dimer
B
RBD Binding Interface
RAS Binding Interface
KRAS
E37
D38
D33
E31
RBD
K183
R188
R158
R166
MEK
14-3-3
KD
C
FP (mP)
KD= 0.085 ± 0.015 μM
BRAF:14-3-32:MEK (μM)
KD= 0.127 ± 0.028 μM
BRAF:14-3-32 (μM)
D
Halo-KRASG12V Pull-down
BRAF:14-3-32:MEK
BRAF:14-3-32
Probe:
BRAF
Halo-KRAS
Total BRAF
E
Halo-KRASG12V Pull-down
WT
R158A
R166A
K183A
R188L
F
RAS
RBD
14-3-3
Different orientations
RAS – 14-3-3 steric clash
β2
α1
SI
α8
α9
M187
M186
RAS – 14-3-3 electrostatic repulsion
D197
E198
D307

Figure 4

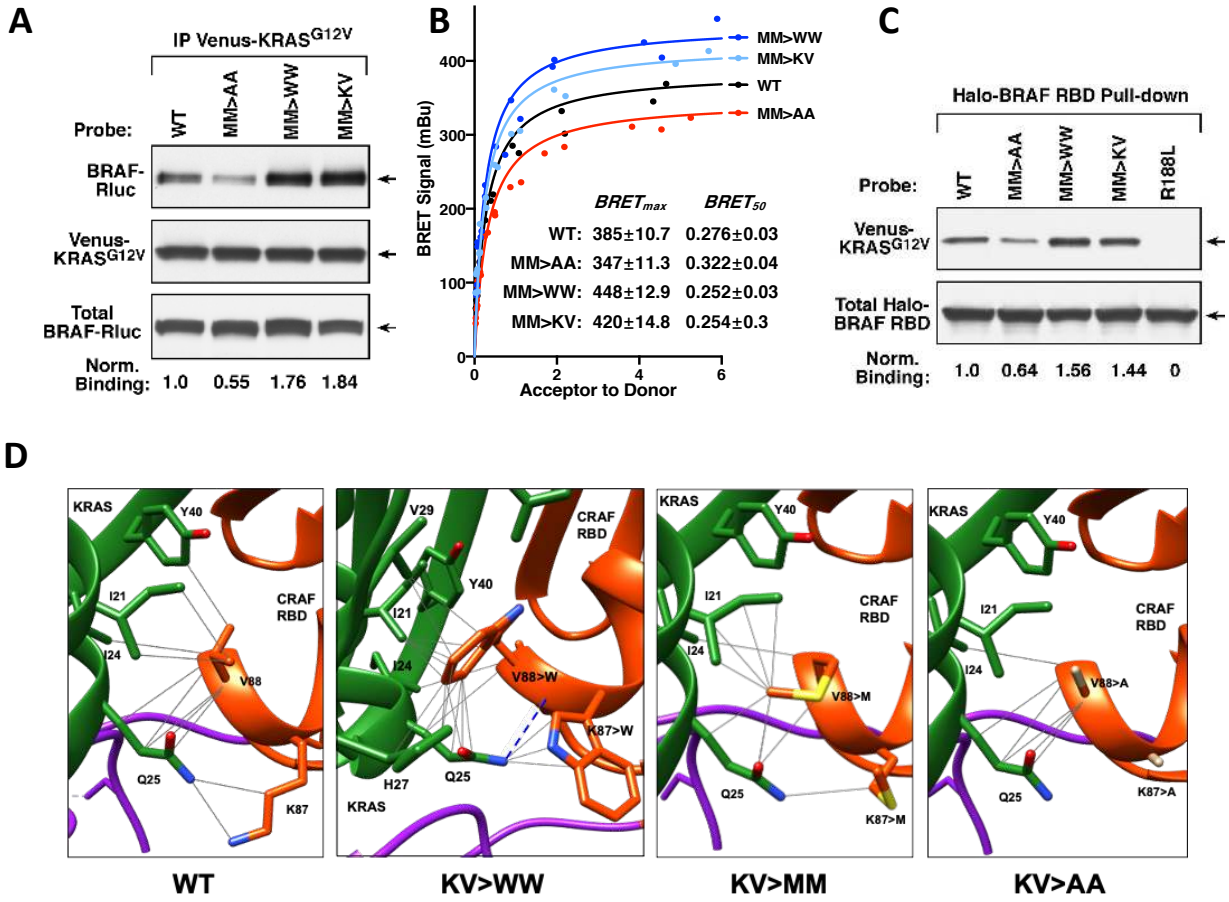
A
IP Venus-KRAS^{G12V}
Probe:
WT
MM>AA
MM>WW
MM>KV
BRAF-Rluc
Venus-KRAS^{G12V}
Total BRAF-Rluc
Norm. Binding: 1.0 0.55 1.76 1.84
B
BRET Signal (mBu)
Acceptor to Donor
MM>WW
MM>KV
WT
MM>AA
BRET$_{max}$ BRET$_{50}$
WT: 385±10.7 0.276±0.03
MM>AA: 347±11.3 0.322±0.04
MM>WW: 448±12.9 0.252±0.03
MM>KV: 420±14.8 0.254±0.3
C
Halo-BRAF RBD Pull-down
Probe:
WT
MM>AA
MM>WW
MM>KV
R188L
Venus-KRAS^{G12V}
Total Halo-BRAF RBD
Norm. Binding: 1.0 0.64 1.56 1.44 0
D
KRAS
Y40
I21
I24
CRAF RBD
V88
Q25
K87
V29
H27
V88>W
K87>W
V88>M
K87>M
V88>A
K87>A
WT
KV>WW
KV>MM
KV>AA

Figure 5

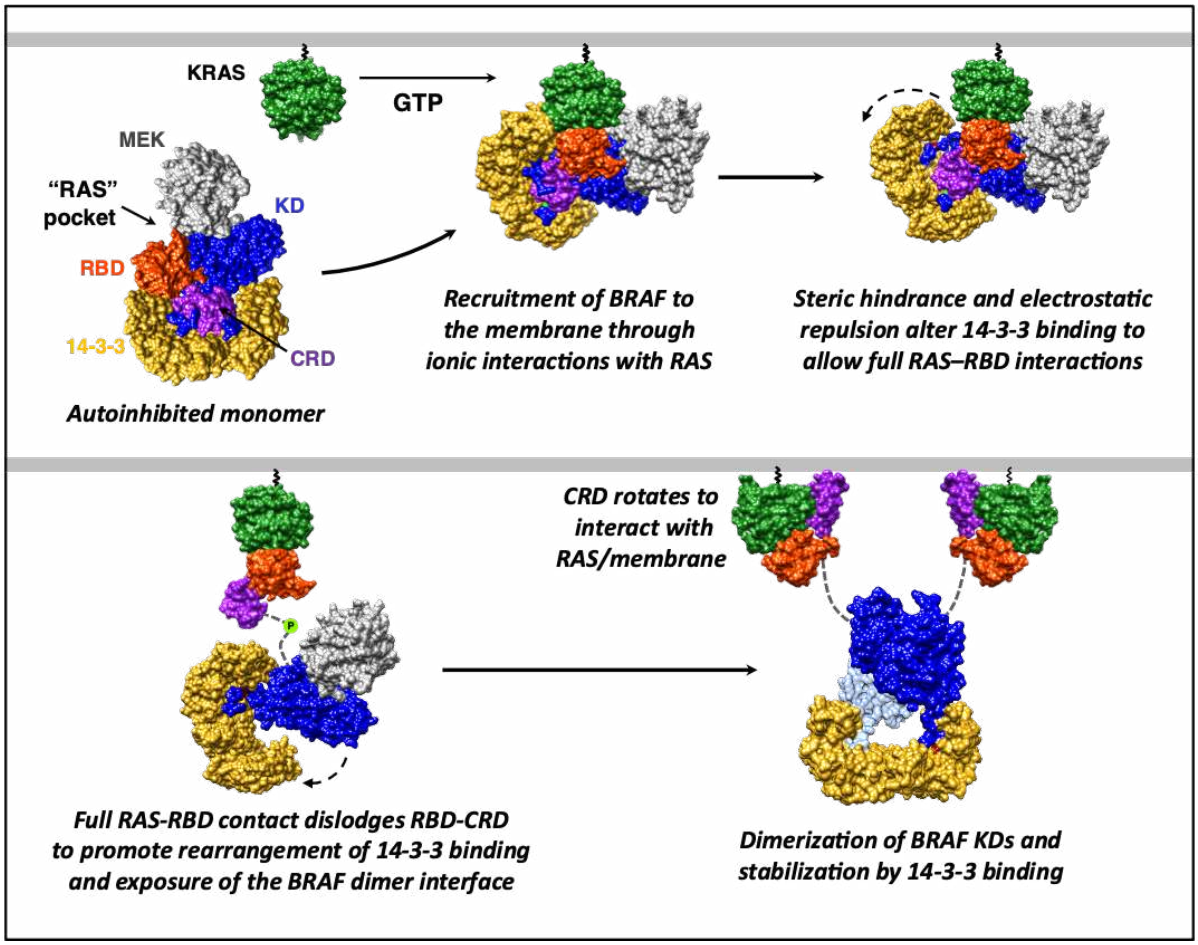
KRAS
GTP
MEK
"RAS" pocket
KD
RBD
14-3-3
CRD
Autoinhibited monomer
Recruitment of BRAF to the membrane through ionic interactions with RAS
Steric hindrance and electrostatic repulsion alter 14-3-3 binding to allow full RAS–RBD interactions
CRD rotates to interact with RAS/membrane
Full RAS-RBD contact dislodges RBD-CRD to promote rearrangement of 14-3-3 binding and exposure of the BRAF dimer interface
Dimerization of BRAF KDs and stabilization by 14-3-3 binding

Figure Legends

Figure 1. Cryo-EM Structure of Inhibitor-bound $BRAF_2$:14-3-3_2 Dimer Complex

(A) BRAF domain organization is shown with color coding: RAS binding domain (RBD, red orange), cysteine-rich domain (CRD, purple), and the kinase domain (KD, blue). BRAF residues S365 (green) and S729 (dark red) serve as 14-3-3 binding sites when phosphorylated.

(B) Cryo-EM density map at 3.9 Å resolution (left) and structure (right) of the $BRAF_2$:14-3-3_2 complex. BRAF domains are colored as in (A), with one KD protomer in light blue and the other in dark blue. SB590885 is shown in coral and the 14-3-3 dimer is colored gold.

(C) Superposition of the SB590885-liganded $BRAF_2$:14-3-3_2 structure (colored as in B) with the previously reported cryo-EM structure of the unliganded $BRAF_2$:14-3-3_2 complex in gray (PDB ID: 6UAN) is shown with a Cα RMSD of 1.03 Å. The inset demonstrates that residues F743-A749 in the C-tail end (in red) of the unliganded complex (PDB ID: 6UAN) and the BRAF inhibitor SB590885 (in coral) in the present structure occupy overlapping positions in the active site.

See also Figure S1 and S2.

Figure 2. Structures of the Autoinhibited, Monomeric BRAF:14-3-3_2:MEK and BRAF:14-3-3_2 Complexes and Analysis of the RBD:14-3-3 Interface

(A) Cryo-EM density map at a 3.7 Å resolution (left), structure of BRAF:14-3-3_2:MEK (middle), and cryo-EM structure of BRAF:14-3-3_2 (right) autoinhibited complexes comprised of a full-length BRAF monomer and a 14-3-3 dimer (colored as previously described) and MEK is shown in gray when present.

(B) Region of RBD:14-3-3 contact, with RBD and 14-3-3 residues at the contact interface depicted as light gray and dark gray, respectively. Interacting residues are labeled (top). Electrostatic surface representation of the RBD and 14-3-3, with blue and red representing positively and negatively charged areas, respectively. Regions of contact between the RBD and 14-3-3 lay within the yellow circles (bottom).

(C) The 14-3-3 α8-helix, α9-helix, and the connecting loop 8 contact the α1-helix and loop 3 of the B-Raf RBD. The RBD is colored in orange, 14-3-3 in gold and the interacting residues are labeled (top). Sequence alignment of RBD residues in the α1-helix and loop 3 of human BRAF, CRAF and ARAF (bottom). Residues at the RBD:14-3-3 interface are denotated by the shaded gray box, and identically conserved residues are shown in red. Symbols under the alignment denotate the degree of conservation as follows: (*) indicates positions which have a fully conserved residue, (:) indicates conservation between groups with strongly similar properties, and (.) indicates conservation between groups with weakly similar properties.

(D) NanoBRET assay monitoring the interaction between WT or mutant $BRAF^{REG}$-Halo proteins and Nano-$BRAF^{KD}$ in live cells to determine the effect of the indicated mutations on the ability of BRAF to form a stable, autoinhibited complex. Data represent BRET signals (normalized to WT set at 100) of quadruplicate wells from 3 independent experiments, with mean ± SD shown.

(E) Lysates of 293FT cells transiently expressing Nano-WT-$BRAF^{KD}$ alone or co-expressing Nano-WT-$BRAF^{KD}$ with increasing amounts of WT- or M186A/M187A-$BRAF^{REG}$-Halo were examined by immunoblot analysis for WT-$BRAF^{REG}$-Halo, Nano-WT-$BRAF^{REG}$, and pMEK levels.

(F) NIH-3T3 cells were infected with retroviruses encoding the indicated WT or mutant FLAG-$BRAF^{FL}$ proteins. Three weeks post-infection, foci were visualized by methylene blue staining. Focus forming assays were repeated 3 times with similar results.

See also Figure S1, S3 and S4.

Figue 3. RAS, BRAF RBD, and 14-3-3 Interactions

(A) Superimposition of KRAS (from KRAS:CRAF_RBD structure PDB ID: 6XI7, colored in green) onto the autoinhibited BRAF:14-3-3_2:MEK complex is shown to demonstrate the fit of KRAS into the "RAS pocket" for RAS:RBD binding.

(B) Electrostatic surface representation of the RAS:RBD binding interface (yellow circle), with critical ionic bond forming residues indicated on the surfaces of KRAS (PDB ID: 6XI7, left) and the RBD of the BRAF:14-3-3_2:MEK complex (right).

(C) Binding affinities of the BRAF:14-3-3_2:MEK (top) and BRAF:14-3-3_2 (bottom) complexes to KRAS(GppNHp) were determined in fluorescence polarization assays. Data are represented as the mean of triplicate wells ± SD. The reported K_D is the mean of three independent experiments.

(D) Purified BRAF:14-3-3_2:MEK and BRAF:14-3-3_2 complexes were evaluated for their ability to bind Halo-tagged $KRAS^{G12V}$ in pull-down assays.

(E) WT or BRAF full-length proteins containing mutations in key basic RBD residues mediating ionic bond interactions with RAS were examined for binding to Halo-$KRAS^{G12V}$ in pull-down assays.

(F) Superimposition of KRAS onto the autoinhibited BRAF:14-3-3_2:MEK complex indicates potential steric clash and electrostatic repulsion between RAS and the 14-3-3 protomer at the RBD:14-3-3 interface upon full RAS:RBD contact. The steric clash (top insets) would occur between RAS α1-helix, switch I (SI) and β2 sheet (ribbon and surface in green) and the α8- and α9- helices of 14-3-3 (ribbon in gold). In the same region, similarly charged residues in KRAS, D30 and E31, and 14-3-3, D197 and D198, would cause electrostatic repulsion (bottom inset, RAS ribbon structure in green superimposed onto the electrostatic surface representation of the RBD and 14-3-3).

See also Figure S4.

Figure 4. RBD Residues at the 14-3-3 Interface Contribute to RAS Binding

(A) WT-BRAF-Rluc and the indicated M186/M187 mutants were assessed for binding to Venus-$KRAS^{G12V}$ in co-immunoprecipitation assays. Lysates were also monitored for BRAF-Rluc protein levels.

(B) BRET saturation curves are shown examining the interaction of WT- or M186/ M187 mutant BRAF-Rluc proteins withVenus-KRAS^{G12V} in live cells. $BRET_{max}$ and $BRET_{50}$ values are listed ± standard error. Saturation curves were repeated 3 times with similar results.

(C) Binding of Venus-KRAS^{G12V} to WT or mutant Halo-BRAF RBD proteins was assessed in pulldown assays. As a control, an RBD protein containing the R188L mutation that disrupts the RAF-RAS interaction was also evaluated.

(D) Modeling the effect of substituting the CRAF K87/V88 amino acids for K87W/V88W, K87/V88 or K87A/V88A in the RBD:RAS structure (KRAS:CRAF_RBD_CRD structure PDB ID: 6XI7, colored in green for KRAS, orange for CRAF RBD and violet for CRAF CRD). Blue dashed and gray lines indicate potential hydrogen bond and other non-electrostatic interactions, respectively.

See also Figure S4.

Figure 5. Model for BRAF monomer to dimer transition. Upon RAS activation, the autoinhibited BRAF monomer is recruited to the plasma membrane through direct ionic interactions between the BRAF RBD and the switch I region of RAS. As RAS forms the full spectrum of RBD contacts, steric clashes and electrostatic repulsion occur between RAS and 14-3-3, resulting in conformational rearrangements that dislodge the RBD/CRD and expose the BRAF dimer interface. The dislodged CRD rotates to interact with the membrane and RAS to further stabilize the interaction. The exposed KD can then dimerize and assume the active catalytic conformation that is stabilized by a 14-3-3 dimer that spans the pS729 sites.

Star Methods

Lead Contact and Materials Availability

Further information and requests for resources and reagents should be directed to and will be fulfilled by the Lead Contacts, Deborah Morrison (morrisod@mail.nih.gov) and Ping Zhang

(ping.zhang@nih.gov). Plasmids and cell lines are available for use upon request to the Lead Contacts.

Experimental Model and Subject Details

Cell Lines and Culture Conditions

293FT, 293T, HeLa, NIH-3T3 and Phoenix-Eco cells were cultured in DMEM supplemented with 10% fetal bovine serum (FBS), 2 mM L-glutamine, and 1% penicillin/streptomycin. All cells were cultured at 37ºC with 5% CO_2.

Methods Details

Generation of Recombinant Lentivirus and Stable 293FT Cells Expressing Halo-BRAF^{WT}

Recombinant lentivirus particles were generated by co-transfecting psPAX2 and pMD2 with the pLenti Halo-BRAF^{WT} construct into 293T cells using the X-tremeGENE9 transfection reagent. 72 hours post-transfection, the virus-containing supernatant was collected, centrifuged twice at 2,000 rpm for 10 minutes to remove any cellular debris, and then stored at -80°C. 293FT cells were infected with viral supernatants containing 8 μg/mL polybrene for 24 hours, following which growth media containing 2μg/mL puromycin (selection media) was added. The selection media was changed every 3 days until resistant cells were obtained.

Affinity Purification of BRAF Complexes and Size Exclusion Chromatography

Halo-BRAF^{WT} 293FT cells were plated into 45 10 cm tissue culture dishes at a concentration of $2x10^6$ cells/dish and allowed to grow to confluence (~3 days after plating). For BRAF monomer samples, media was left unchanged until collection to allow for serum-depletion. For BRAF dimer samples, media was replaced the day prior to collection with fresh growth media containing 2μM SB590885. On the day of collection, media was removed by suction from each plate and the cells were washed twice with 5 ml cold PBS. Cells were then lysed in Triton lysis buffer (1% Triton X-100, 137 mM NaCl, 20 mM Tris pH 8.0, 0.15 U/mL aprotinin, 1 mM phenylmethylsulfonyl fluoride, 20 μM leupeptin; 0.5 mM sodium vanadate; 1mL per 10 cm dish) at 4ºC for 15 minutes

on a rocking platform. Lysates were collected and clarified of debris by centrifugation at 14,000 rpm for 10 min at 4°C.

To isolate the BRAF complexes, 5 mL of Halolink resin (Promega) was washed twice with Triton X-100 lysis buffer prior to the addition of lysate. The samples were then incubated for 2 hours at 4°C on a rocking platform. Beads containing the bound BRAF complexes were washed twice with Triton X-100 lysis buffer and three times with elution buffer (137mM NaCl, 20mM Tris pH 8). The bead-bound complexes were then resuspended in 2.5ml elution buffer containing 50µl Halo-TEV (Promega) and incubated for 2 hours at 4°C on a rocking platform. Beads were then pelleted and supernatant containing the eluted BRAF complexes were applied to a Superdex 6 Increase 10/300 GL column (Cytiva) preequilibrated with 20 mM Tris pH 8.0, 137 mM NaCl. Proteins from the peak fractions corresponding to BRAF complexes were collected and analyzed by SDS-PAGE and silver staining.

Cryo-EM Grid Preparation, Data Acquisition, and Processing

After gel filtration, the BRAF:14:3-3_2:MEK, BRAF:14-3-3_2 and $BRAF_2$:14-3-3_2 complexes (in 20 mM Tris pH 8.0 and 137 mM NaCl) were concentrated to 0.18 - 0.20 mg/ml by centrifugation in a 30K pore size Pall's Microsep™ advance centrifugal device. The samples were supplemented with NaCl and DTT to a final concentration of 200 mM and 10 mM, respectively, before freezing. Quantifoil Au R 1.2/1.3 holey carbon girds were glow-discharged for 45 sec at 20 mA in alcohol environment. A volume of 1.5 µl of protein solution was applied to each side of the grids, and the samples were vitrified in a FEI Vitrobot Mark IV, using a force of 10 au and a blotting time of 1.5 to 2.0 seconds at 4 °C with humidity >85%. The samples were then frozen by plunge-freezing the grids into liquid ethane cooled to approximately -180°C by liquid nitrogen. 50 frames per movie were collected from the frozen hydrated samples at a nominal magnification of 130,000x for the BRAF:14:3-3_2:MEK sample (corresponding to 1.058 Å per physical pixel) using a Titan Kiros electron microscope (FEI) at 300kV with a K2 summit direct detection camera (Gatan) in super-resolution mode. The slit width of the energy filter was set to 20 eV. Then, using SerialEM [40]

data collection software, the micrographs were dose-fractionated into 50 frames with a total exposure time of 8s and a total electron exposure of 57 electrons per Å^2, with defocus values ranging from -0.8 to -2.5 μM.

All cryo-EM data analysis was done using RELION 3.1 [41]. For the BRAF:14:3-3$_2$:MEK complex, a total of 3,976 micrographs were collected. The raw movies were aligned and gain corrected to compensate for sample movement and drift by MotionCor2 [42] with 5 by 5 patches and a B-factor of 150. The Gctf program [43] was used to estimate the contrast transfer function (CTF) parameters of each motion-corrected image. The micrographs were screened to remove low-quality images and those with unqualified CTF power spectra. An initial set of particles were manually picked and used to generate 2D class templates for automatic particle picking, using a box size of 180 pixels. Particle selection was inspected to remove any contaminants and to add missed particles. The resulting particles were subjected to three rounds of 2D classification to identify and discard false positives or other apparent contaminants. Following 2D classification, particles were further selected, re-centered, and re-extracted for 3D classification. An initial model was generated and, based on structural integrity and map quality of complex, the best 3D class was then used for 3D refinement. After 3D auto-refinement, Bayesian polishing and per-particle CTF refinements were applied, until the 3D refinement converged. The final map was sharpened using a B-factor of -100.5 Å^2, yielding a density map at a resolution of 3.7 Å, based on the gold standard FSC 0.143 criteria. Masked-based local refinement was also performed on the BRAF KD:MEK portion of the structure, which generated a density map with the same resolution and quality, and on the BRAF KD portion of the structure, which resulted in no further improvement of the map.

The monomeric BRAF:14-3-3$_2$ and dimeric BRAF$_2$:14-3-3$_2$ datasets were collected in a similar manner, with 50 frames per movie collected from the frozen hydrated samples at a nominal magnification of 105,000x (corresponding to 1.348 Å per physical pixel). The micrographs were dose-fractionated into 50 frames every 0.2s with a dose rate of 5.5 e-/Å^2/s, total exposure time of

10s and an accumulated dose of 55 electrons per Å^2. The datasets were further processed in the same manner as described for the BRAF:14-3-3$_2$:MEK dataset Table S1.

Models for the autoinhibited BRAF complexes were built by rigid-body fitting of the individual BRAF domains using PDB IDs 5J17 for the RBD [44], 1FAR for the CRD [45], 4MNE for the KD [46], and 3WIG [47] for MEK1 protomer, when present. Similarly, the active BRAF dimer complex was built by rigid-body fitting using PDB ID 2FB8 [48] for the BRAF KD. For all structures, 14-3-3 was built by rigid-body fitting using 14-3-3ζ PDB ID 4FJ3 [49]. Each subunit of 14-3-3 dimer was fit individually, and the BRAF pS365 and pS729 sites were built manually as were any additional residues needed. Fitting of the models into their respective maps was initially done using USCF Chimera [50]. Manual adjustment of the model was performed in Coot [51], followed by iterative rounds of real space refinement in Phenix [52] and manual fitting in Coot. Model validation was done using statistics from Ramachandran plots and MolProbity scores in Phenix and Coot. Statistics for the final refinements are shown in Table S1. Figures were generated by USCF Chimera. Structure deviations and electrostatic potential of surfaces were calculated using MatchMaker and Columbic Surface plugins, respectively, in USCF Chimera.

Initial diagnostic data sets for the three BRAF complexes were collected on a Talos Arctica microscope (FEI) at 200Kv with a Gatan K3 summit direct detection camera at either the NCI-Frederick cryo-EM Facility or at the John M. Cowley Center for High Resolution Electron Microscopy, Arizona State University. As mentioned earlier, data for generating the structures with the final reported resolutions was collected on a Titan Krios microscope at 300kV with a Gatan K2 summit direct detection camera in super-resolution mode.

Fluorescence Polarization Assay

Fluorescence polarization assay was used to measure the binding of BRAF:14-3-3$_2$:MEK and BRAF:14-3-3$_2$ complexes to KRAS. GppNHp-loaded GFP-KRAS at concentration of 0.73 nM was mixed with 0.0057-2.4 μM of BRAF:14-3-3$_2$:MEK and BRAF:14-3-3$_2$ complexes in buffer containing 20 mM Tris pH 8.0 and 137mM NaCl. Fluorescence polarization of the samples was

measured in black flat-bottom assay plates (Corning) using a CLARIOstar micro-plate reader (BMG LABTECH) with 482 nm excitation and 540 nm emission. The data was analyzed and fitted to the anisotropy single association hyperbolic equation using Prism 8 software.

NanoBRET RAF Autoinhibition Assay

293FT cells were seeded into 6-well tissue culture plates at a concentration of $4x10^5$ cells/well. 16 hours after plating, cells were co-transfected using 5 ng of the indicated NanoLuc-RAF^{CAT} construct and 20 ng of the indicated $BRAF^{REG}$-Halo construct (per well). Twenty-four hours later, cells were collected and resuspended in serum-free/phenol free Opti-MEM (Gibco). 1 µl/ml HaloTag NanoBRET 618 ligand was added to the cell suspension and cells were seeded at a concentration of 8 $x10^3$ cells per well of a 384-well plate (BioTek) in quadruplicate, with the remaining cells plated into a fresh 6-well tissue culture plate. After 24 hours, 10 µl/ml NanoBRET™ NanoGlo substrate was added to each well of cells to be monitored for NanoBRET, and donor (460nm) and acceptor (618nm) emissions were measured using a Perkins Elmer Envision plate reader (#2104-0010A containing a 460nm/50nm emission filter and a 610nm LP filter). Cells seeded into the 6-well plates were lysed and examined by immunoblot analysis using αHalo-tag (for RAF^{REG} detection) and αNanoLuc (for RAF^{CAT} detection) to ensure equal expression levels across conditions.

Transfection, Cell Lysis, and Co-immunoprecipitation Assays

HeLa or 293FT cells were plated into 10 cm tissue culture dishes at a concentration of 0.5 x 10^6/dish, 18-24 hours prior to transfection. Cells were then transfected using the XtremeGENE9 transfection reagent per the manufacturer's instructions, at a 2:1 ratio of XtremeGENE9 to DNA. 30 hours after transfection, cells were serum-starved for 18 hours, prior to lysis. For cell lysis, cells were washed twice with ice cold PBS and lysed in 1% NP-40 buffer (20mM Tris pH 8.0, 137 mM NaCl, 10% glycerol, 1% NP-40 alternative, 0.15 U/mL aprotinin, 1 mM phenylmethylsulfonyl fluoride, 0.5 mM sodium vanadate, 20 µM leupeptin) for 15 min at 4°C on a rocking platform. Lysates were clarified by centrifugation at 14,000 rpm for 10 min at 4°C, following which the

protein content was determined by Bradford assays. Lysates containing equivalent amounts of protein were incubated with the appropriate antibody and protein G sepharose beads for 2 hours at 4°C on a rocking platform. Complexes were washed extensively with 1% NP-40 buffer and then examined by immunoblot analysis, together with aliquots of equalized total cell lysate.

Focus Forming Assay

Recombinant retroviruses expressing the Raf proteins of interest were generated by transfecting a 100 mm tissue culture dish of Phoenix-Eco cells with 6 μg of DNA construct using the XtremeGENE9 protocol described above. Viral supernatants were collected 48 hours post-transfection, centrifuged twice at 1500 rpm for 10 minutes, and either stored at -80°C or used directly. NIH-3T3 cells were plated into 60 mm tissue culture dishes at a concentration of 2 x 10^5 cells/dish. After 16 hours, cells were infected with the indicated recombinant retrovirus in media containing 4% FBS and 8 μg/mL polybrene. 24 hours later, cells were trypsinized and plated into two 100 mm dishes, one of which contained 5 μg/mL puromycin. After 2-4 weeks of culture, cells were fixed with 3.7% formaldehyde and stained with 1% methylene blue.

Pull down Assays Using Halo-RAS or Halo-RBD Beads

For bead preparation, 293FT cells transiently expressing the indicated Halo-$KRAS^{G12V}$ or Halo-RBD constructs were lysed in RIPA lysis buffer (20 mM Tris pH 8.0, 137 mM NaCl, 10% glycerol, 1% NP-40 alternative, 1% SDS, and 0.1% sodium deoxycholate, 0.15 U/mL aprotinin, 1 mM phenylmethylsulfonyl fluoride, 0.5 mM sodium vanadate, 20 mM leupeptin; 1 mL per 10 cm dish) for 15 minutes at 4°C on a rocking platform. Lysates were clarified by centrifugation at 14,000 rpm for 10 min at 4°C. Halolink resin (Promega) was washed twice with RIPA buffer and then added to the lysate (30 μL of bead resin per mL of lysate). Samples were incubated for 2 hours at 4°C on a rocking platform. Beads containing the Halo-tagged proteins were then washed once with RIPA buffer and twice with Triton lysis buffer (1% Triton, 137mM NaCl, 20mM Tris pH 8), prior to resuspension in Triton X-100 lysis buffer.

For pull-down assays using cell lysates, 293FT cells expressing the desired RAS or BRAF proteins were lysed in Triton X-100 lysis buffer, following which the protein content of the lysates was determined by Bradford assays. Lysates containing equivalent amounts of protein were incubated with the Halo-RAS or Halo-RBD beads (30 ul beads per 1 mL lysate) for 1.5 hours at 4°C on a rocking platform. The beads containing the pull-down complexes were washed once with Triton lysis buffer and twice with elution buffer (137mM NaCl, 20mM Tris pH 8). The bead pellet was resuspended in 150 µl elution buffer containing 2µl Halo-TEV (Promega) and incubated for 30 minutes at 4°C. Beads were then pelleted and the eluate collected for immunoblot analysis. Alternatively, for pull-down experiments examining the binding of purified BRAF complexes to $KRAS^{G12V}$, 30µl of washed $KRAS^{G12V}$ beads were incubated with 500µl of the gel filtration fractions for 1.5 hours at 4°C on a rocking platform. Beads were then washed three times with elution buffer and the eluate collected as described above.

BRET RAS-RAF Interaction Assay

293FT cells were seeded into 12-well dishes at a concentration of $1x10^5$ cells/well. 16 hours after plating, Venus-tagged and Rluc8-tagged constructs were co-transfected into cells using a calcium phosphate protocol. A 12-point saturation curve was generated in which the concentration of the energy donor construct (Rluc8) was held constant (62.5 ng) as the concentration of the energy acceptor plasmid (Venus) increased (0-1.0 µg). Cells were collected 48 hours after transfection, washed, and resuspended in PBS (500 µL). 30 µL of the cell suspension was plated in duplicate into wells of a 384-well white-walled plate (PerkinElmer CulturPlate) and coelenterazine-h was added to a final concentration of 3.375 µM. The BRET and Rluc8 emissions were measured simultaneously using a PHERAstar Plus plate reader (BMG Labtech), with BRET monitored at 535 nm (bandwidth 30 nm) and Rluc8 measured at 475 nm (bandwidth 30 nm). 90 µL of the cell suspension was also plated in duplicate into wells of a 96-well black-walled plate (PerkinElmer OptiPlate), and Venus fluorescence was determined using an excitation wavelength of 485 nm (5 nm bandwidth) and the emission monitored at 530 nm (5 nm bandwidth) using a Tecan Infinite

M1000 plate reader. The BRET value for each data point was calculated by dividing the BRET ratio (BRET/Rluc8) by the background signal. The acceptor/donor ratio was equalized against a control where equal quantities of Venus and Rluc8 constructs were transfected. Data was analyzed using GraphPad Prism. Non-linear regression was used to plot the best fit hyperbolic curve and values for $BRET_{max}$ and $BRET_{50}$ were obtained from the calculated best fit curves.

Data and Software Availability

Three-dimensional cryo-EM density maps have been deposited in the Electron Microscopy data Bank under accession numbers EMD-23813 (BRAF:14-3-3_2:MEK), EMD-23814 (BRAF:14-3-3_2), and EMD-23815 ($BRAF_2$:14-3-3_2). The coordinates of atomic models have been deposited in the Protein Data Bank under accession numbers PDB ID: 7MFD (BRAF:14-3-3_2:MEK), 7MFE (BRAF:14-3-3_2), and 7MFF ($BRAF_2$:14-3-3_2). All other relevant data supporting the key findings of this study are available within the article and its supplementary information files or from the corresponding authors upon reasonable request.

References

1 Shaul, Y. D. & Seger, R. The MEK/ERK cascade: from signaling specificity to diverse functions. *Biochimica et biophysica acta* **1773**, 1213-1226, doi:10.1016/j.bbamcr.2006.10.005 (2007).

2 Lavoie, H. & Therrien, M. Regulation of RAF protein kinases in ERK signalling. *Nat Rev Mol Cell Biol* **16**, 281-298, doi:10.1038/nrm3979 (2015).

3 Terrell, E. M. & Morrison, D. K. Ras-mediated activation of the Raf family kinases. *Cold Spring Harb Perspect Med* **9**, doi:10.1101/cshperspect.a033746 (2019).

4 Cox, A. D. & Der, C. J. Ras history: The saga continues. *Small GTPases* **1**, 2-27, doi:10.4161/sgtp.1.1.12178 (2010).

5 Simanshu, D. K., Nissley, D. V. & McCormick, F. RAS proteins and their regulators in human disease. *Cell* **170**, 17-33, doi:10.1016/j.cell.2017.06.009 (2017).

6 Schubbert, S., Shannon, K. & Bollag, G. Hyperactive Ras in developmental disorders and cancer. *Nat Rev Cancer* **7**, 295-308, doi:10.1038/nrc2109 (2007).

7 Fernández-Medarde, A. & Santos, E. Ras in cancer and developmental diseases. *Genes Cancer* **2**, 344-358, doi:10.1177/1947601911411084 (2011).

8 Daum, G., Eisenmann-Tappe, I., Fries, H. W., Troppmair, J. & Rapp, U. R. The ins and outs of Raf kinases. *Trends Biochem Sci* **19**, 474-480. (1994).

9 Nan, X. *et al.* Single-molecule superresolution imaging allows quantitative analysis of RAF multimer formation and signaling. *Proceedings of the National Academy of Sciences of the United States of America* **110**, 18519-18524, doi:10.1073/pnas.1318188110 (2013).

10 Cutler, R. E. J., Stephens, R. M., Saracino, M. R. & Morrison, D. K. Autoregulation of the Raf-1 serine/threonine kinase. *Proc Natl Acad Sci USA* **95**, 9214-9219 (1998).
11 Chong, H. & Guan, K.-L. Regulation of Raf through phosphorylation and N-terminus-C terminus interaction. *J. Biol. Chem.* **278**, 36269-36276 (2003).
12 Tran, N. H., Wu, X. & Frost, J. A. B-Raf and Raf-1 are regulated by distinct autoregulatory mechanisms. *J Biol Chem* **280**, 16244-16253, doi:10.1074/jbc.M501185200 (2005).
13 Park, E. *et al.* Architecture of autoinhibited and active BRAF-MEK1-14-3-3 complexes. *Nature*, doi:10.1038/s41586-019-1660-y (2019).
14 Van Aelst, L., Barr, M., Marcus, S., Polverino, A. & Wigler, M. Complex formation between Ras and Raf and other protein kinases. *Proc. Natl. Acad. Sci. USA* **90**, 6213-6217 (1993).
15 Vojtek, A. B., Hollenberg, S. M. & Cooper, J. A. Mammalian Ras interacts directly with the serine/threonine kinase Raf. *Cell* **74**, 205-214 (1993).
16 Zhang, X. F. *et al.* Normal and oncogenic p21ras proteins bind to the amino-terminal regulatory domain of c-Raf-1. *Nature* **364**, 308-313, doi:10.1038/364308a0 (1993).
17 Marais, R., Light, Y., Paterson, H. F. & Marshall, C. J. Ras recruits Raf-1 to the plasma membrane for activation by tyrosine phosphorylation. *Embo j* **14**, 3136-3145 (1995).
18 Weber, C. K., Slupsky, J. R., Kalmes, H. A. & Rapp, U. R. Active Ras induces heterodimerization of cRaf and BRaf. *Cancer Res* **61**, 3595-3598 (2001).
19 Rushworth, L. K., Hindley, A. D., O'Neill, E. & Kolch, W. Regulation and role of Raf-1/B-Raf heterodimerization. *Mol Cell Biol* **26**, 2262-2272, doi:10.1128/mcb.26.6.2262-2272.2006 (2006).
20 Freeman, A. K., Ritt, D. A. & Morrison, D. K. Effects of Raf dimerization and its inhibition on normal and disease-associated Raf signaling. *Mol Cell* **49**, 751-758, doi:10.1016/j.molcel.2012.12.018 (2013).
21 Hu, J. *et al.* Allosteric activation of functionally asymmetric RAF kinase dimers. *Cell* **154**, 1036-1046, doi:10.1016/j.cell.2013.07.046 (2013).
22 Marshall, C. J. MAP kinase kinase kinase, MAP kinase kinase and MAP kinase. *Current opinion in genetics & development* **4**, 82-89, doi:10.1016/0959-437x(94)90095-7 (1994).
23 Kondo, Y. *et al.* Cryo-EM structure of a dimeric B-Raf:14-3-3 complex reveals asymmetry in the active sites of B-Raf kinases. *Science* **366**, 109-115, doi:10.1126/science.aay0543 (2019).
24 Liau, N. P. D. *et al.* Dimerization Induced by C-Terminal 14-3-3 Binding Is Sufficient for BRAF Kinase Activation. *Biochemistry* **59**, 3982-3992, doi:10.1021/acs.biochem.0c00517 (2020).
25 Guan, K.-L. *et al.* Negative regulation of the serine/threonine kinase B-Raf by Akt. *J. Biol. Chem.* **275**, 27354-27359 (2000).
26 Freeman, A. K. & Morrison, D. K. 14-3-3 Proteins: diverse functions in cell proliferation and cancer progression. *Semin Cell Dev Biol* **22**, 681-687, doi:10.1016/j.semcdb.2011.08.009 (2011).
27 Liau, N. P. D. *et al.* Negative regulation of RAF kinase activity by ATP is overcome by 14-3-3-induced dimerization. *Nat Struct Mol Biol* **27**, 134-141, doi:10.1038/s41594-019-0365-0 (2020).
28 Rajakulendran, T., Sahmi, M., Lefrancois, M., Sicheri, F. & Therrien, M. A dimerization-dependent mechanism drives RAF catalytic activation. *Nature* **461**, 542-545, doi:10.1038/nature08314 (2009).

29 McClendon, C. L., Kornev, A. P., Gilson, M. K. & Taylor, S. S. Dynamic architecture of a protein kinase. *Proceedings of the National Academy of Sciences of the United States of America* **111**, E4623-4631, doi:10.1073/pnas.1418402111 (2014).
30 Thevakumaran, N. *et al.* Crystal structure of a BRAF kinase domain monomer explains basis for allosteric regulation. *Nat Struct Mol Biol* **22**, 37-43, doi:10.1038/nsmb.2924 (2015).
31 Peng, S. B. *et al.* Inhibition of RAF Isoforms and Active Dimers by LY3009120 Leads to Anti-tumor Activities in RAS or BRAF Mutant Cancers. *Cancer Cell* **28**, 384-398, doi:10.1016/j.ccell.2015.08.002 (2015).
32 Karoulia, Z. *et al.* An Integrated Model of RAF Inhibitor Action Predicts Inhibitor Activity against Oncogenic BRAF Signaling. *Cancer Cell* **30**, 485-498, doi:10.1016/j.ccell.2016.06.024 (2016).
33 Fischmann, T. O. *et al.* Crystal structures of MEK1 binary and ternary complexes with nucleotides and inhibitors. *Biochemistry* **48**, 2661-2674, doi:10.1021/bi801898e (2009).
34 Nassar, N. *et al.* The 2.2 A crystal structure of the Ras-binding domain of the serine/threonine kinase c-Raf1 in complex with Rap1A and a GTP analogue. *Nature* **375**, 554-560, doi:10.1038/375554a0 (1995).
35 Herrmann, C., Martin, G. A. & Wittinghofer, A. Quantitative analysis of the complex between p21ras and the Ras-binding domain of the human Raf-1 protein kinase. *J Biol Chem* **270**, 2901-2905. (1995).
36 Fetics, S. K. *et al.* Allosteric effects of the oncogenic RasQ61L mutant on Raf-RBD. *Structure* **23**, 505-516, doi:10.1016/j.str.2014.12.017 (2015).
37 Tran, T. H. *et al.* KRAS interaction with RAF1 RAS-binding domain and cysteine-rich domain provides insights into RAS-mediated RAF activation. *Nat Commun* **12**, 1176, doi:10.1038/s41467-021-21422-x (2021).
38 Terrell, E. M. *et al.* Distinct binding preferences between Ras and Raf family members and the impact on oncogenic Ras signaling. *Mol Cell* **76**, 872-884 e875, doi:10.1016/j.molcel.2019.09.004 (2019).
39 Cookis, T. & Mattos, C. Crystal structure reveals the full Ras:Raf interface and advances mechanistic understanding of Raf activation. *bioRxiv*, 2020.2007.2028.225938, doi:10.1101/2020.07.28.225938 (2020).
40 Mastronarde, D. N. Automated electron microscope tomography using robust prediction of specimen movements. *J Struct Biol* **152**, 36-51, doi:10.1016/j.jsb.2005.07.007 (2005).
41 Zivanov, J. *et al.* New tools for automated high-resolution cryo-EM structure determination in RELION-3. *Elife* **7**, doi:10.7554/eLife.42166 (2018).
42 Zheng, S. Q. *et al.* MotionCor2: anisotropic correction of beam-induced motion for improved cryo-electron microscopy. *Nat Methods* **14**, 331-332, doi:10.1038/nmeth.4193 (2017).
43 Zhang, K. Gctf: Real-time CTF determination and correction. *J Struct Biol* **193**, 1-12, doi:10.1016/j.jsb.2015.11.003 (2016).
44 Athuluri-Divakar, S. K. *et al.* A Small Molecule RAS-Mimetic Disrupts RAS Association with Effector Proteins to Block Signaling. *Cell* **165**, 643-655, doi:10.1016/j.cell.2016.03.045 (2016).
45 Mott, H. R. *et al.* The solution structure of the Raf-1 cysteine-rich domain: a novel ras and phospholipid binding site. *Proceedings of the National Academy of Sciences of the United States of America* **93**, 8312-8317 (1996).

46 Haling, J. R. *et al.* Structure of the BRAF-MEK complex reveals a kinase activity independent role for BRAF in MAPK signaling. *Cancer Cell* **26**, 402-413, doi:10.1016/j.ccr.2014.07.007 (2014).
47 Lito, P. *et al.* Disruption of CRAF-mediated MEK activation is required for effective MEK inhibition in KRAS mutant tumors. *Cancer Cell* **25**, 697-710, doi:10.1016/j.ccr.2014.03.011 (2014).
48 King, A. J. *et al.* Demonstration of a genetic therapeutic index for tumors expressing oncogenic BRAF by the kinase inhibitor SB-590885. *Cancer Res* **66**, 11100-11105, doi:10.1158/0008-5472.Can-06-2554 (2006).
49 Molzan, M. & Ottmann, C. Synergistic binding of the phosphorylated S233- and S259-binding sites of C-RAF to one 14-3-3ζ dimer. *J Mol Biol* **423**, 486-495, doi:10.1016/j.jmb.2012.08.009 (2012).
50 Pettersen, E. F. *et al.* UCSF Chimera--a visualization system for exploratory research and analysis. *J Comput Chem* **25**, 1605-1612, doi:10.1002/jcc.20084 (2004).
51 Emsley, P. & Cowtan, K. Coot: model-building tools for molecular graphics. *Acta Crystallogr D Biol Crystallogr* **60**, 2126-2132, doi:10.1107/s0907444904019158 (2004).
52 Adams, P. D. *et al.* PHENIX: a comprehensive Python-based system for macromolecular structure solution. *Acta Crystallogr D Biol Crystallogr* **66**, 213-221, doi:10.1107/s0907444909052925 (2010).

Supplemental Materials

Structural Insights into the BRAF Monomer-to-dimer Transition Mediated by RAS Binding

Juliana A. Martinez Fiesco[1*], David E. Durrant[2*], Deborah K. Morrison[2^]

and Ping Zhang[1^]

[1]Center for Structural Biology and [2]Laboratory of Cell and Developmental Signaling, Center for Cancer Research, National Cancer Institute-Frederick, Frederick, MD 21702

* These authors contributed equally to this work

^ *corresponding authors: morrisod@mail.nih.gov and ping.zhang@nih.gov

Supplemental Materials:

Supplemental Figures S1-S4

Supplemental Figure Legends S1-S4

Supplemental Table S1-S2

Supplemental Figures

Figure S1

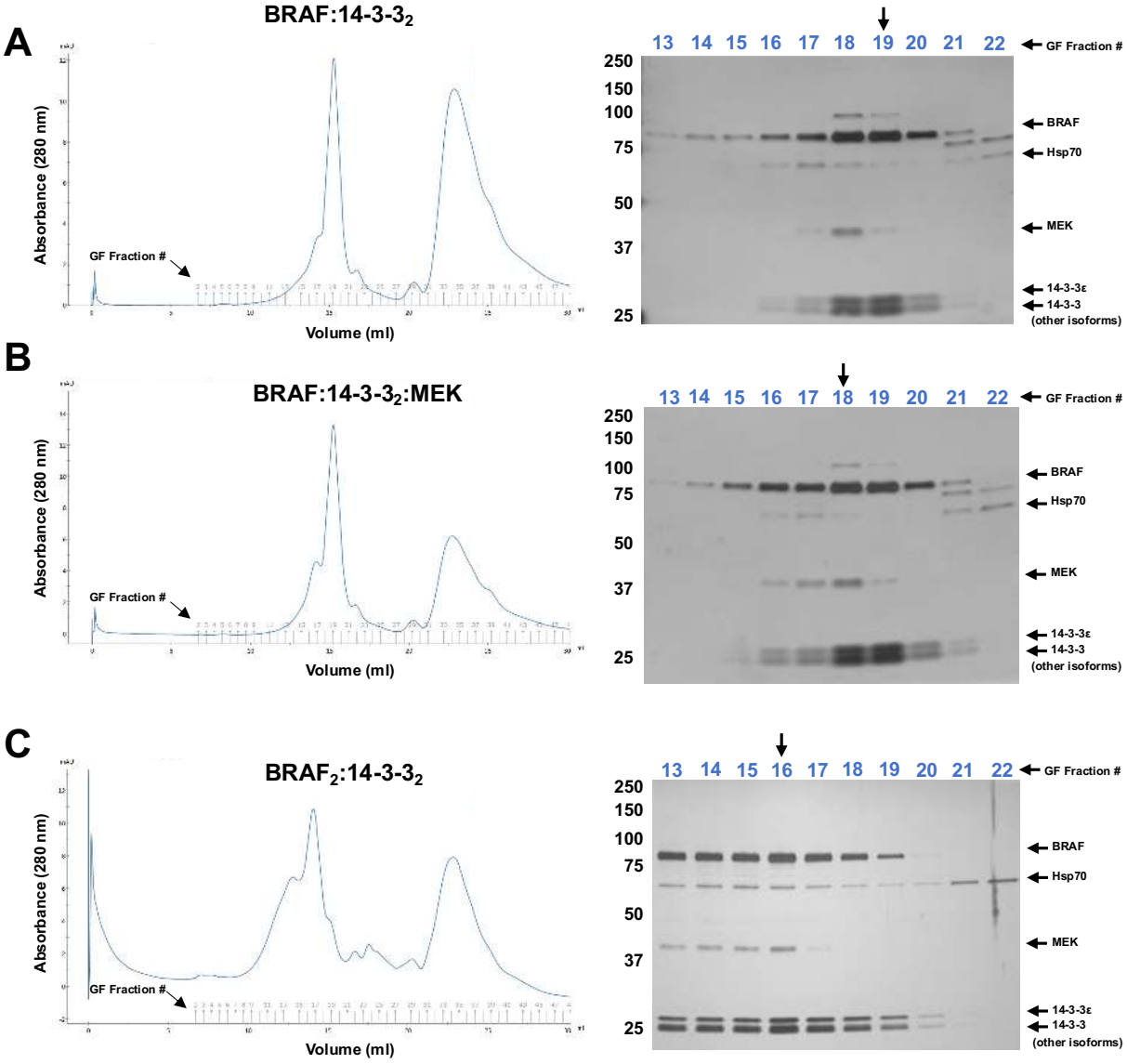

D

Protein	Accession	BRAF:14-3-3$_2$:MEK	BRAF:14-3-3$_2$	BRAF$_2$:14-3-3$_2$
14-3-3 protein epsilon	P62258	51.5	51.2	43.5
14-3-3 protein zeta/delta	P63104	22.5	24.7	25.8
14-3-3 protein beta/alpha	P31946	8.8	8.1	9.5
14-3-3 protein eta	Q04917	6.4	6.4	9.6
14-3-3 protein gamma	P61981	6	5.9	3.9
14-3-3 protein theta	P27348	4.5	3.6	7
14-3-3 protein sigma	P31947	0.3	0.1	0.7
MEK1	Q02750	53.6		
MEK2	P36507	46.4		

Values represent percentage of total peptides for 14-3-3 or MEK

Figure S2

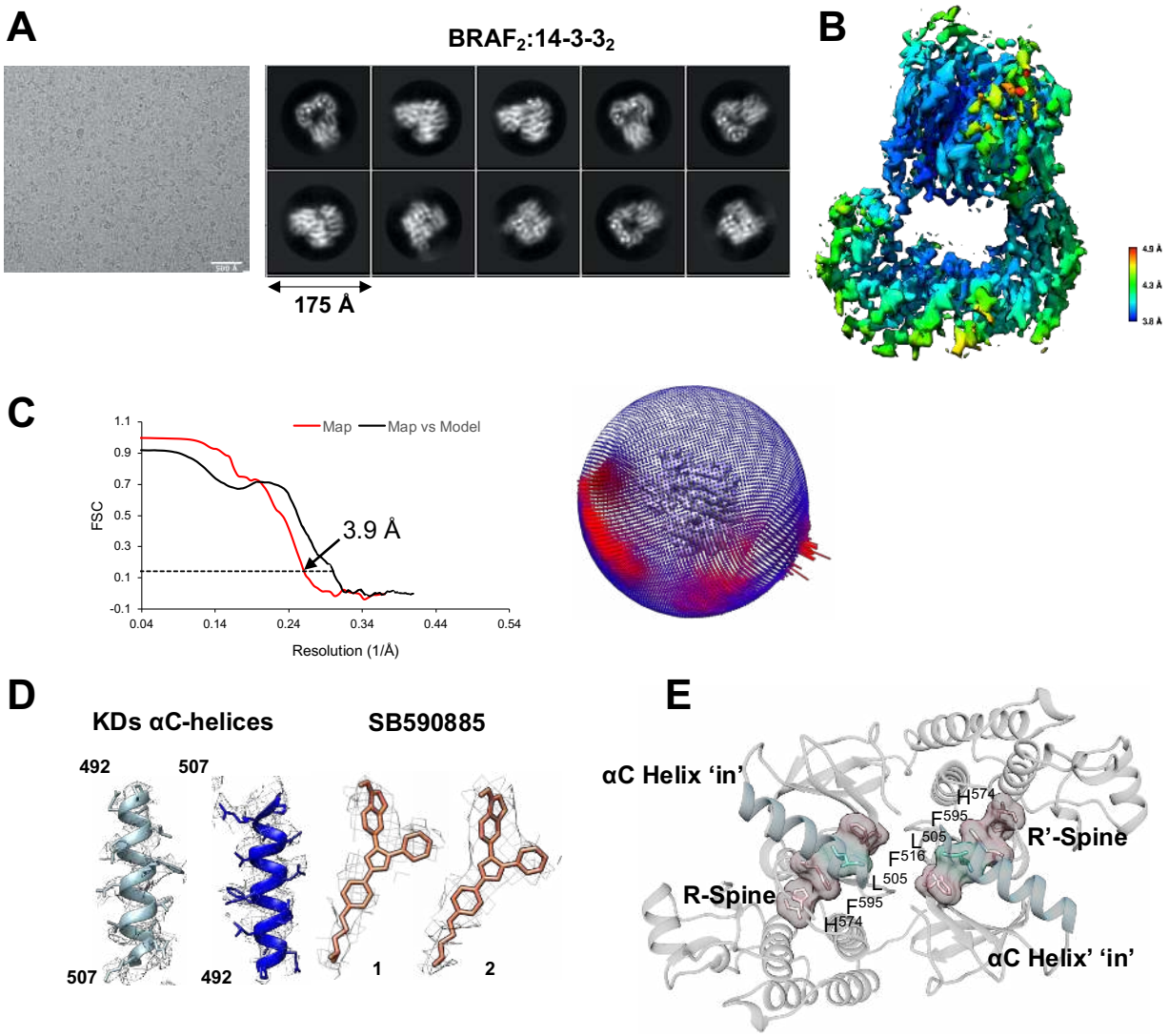
A
BRAF2:14-3-32
175 Å
B
4.9 Å
4.3 Å
3.8 Å
C
Map
Map vs Model
FSC
3.9 Å
Resolution (1/Å)
D
KDs αC-helices
SB590885
492
507
507
492
1
2
E
αC Helix 'in'
H574
F595
L505
R'-Spine
F516
L505
R-Spine
F595
H574
αC Helix' 'in'

Figure S3

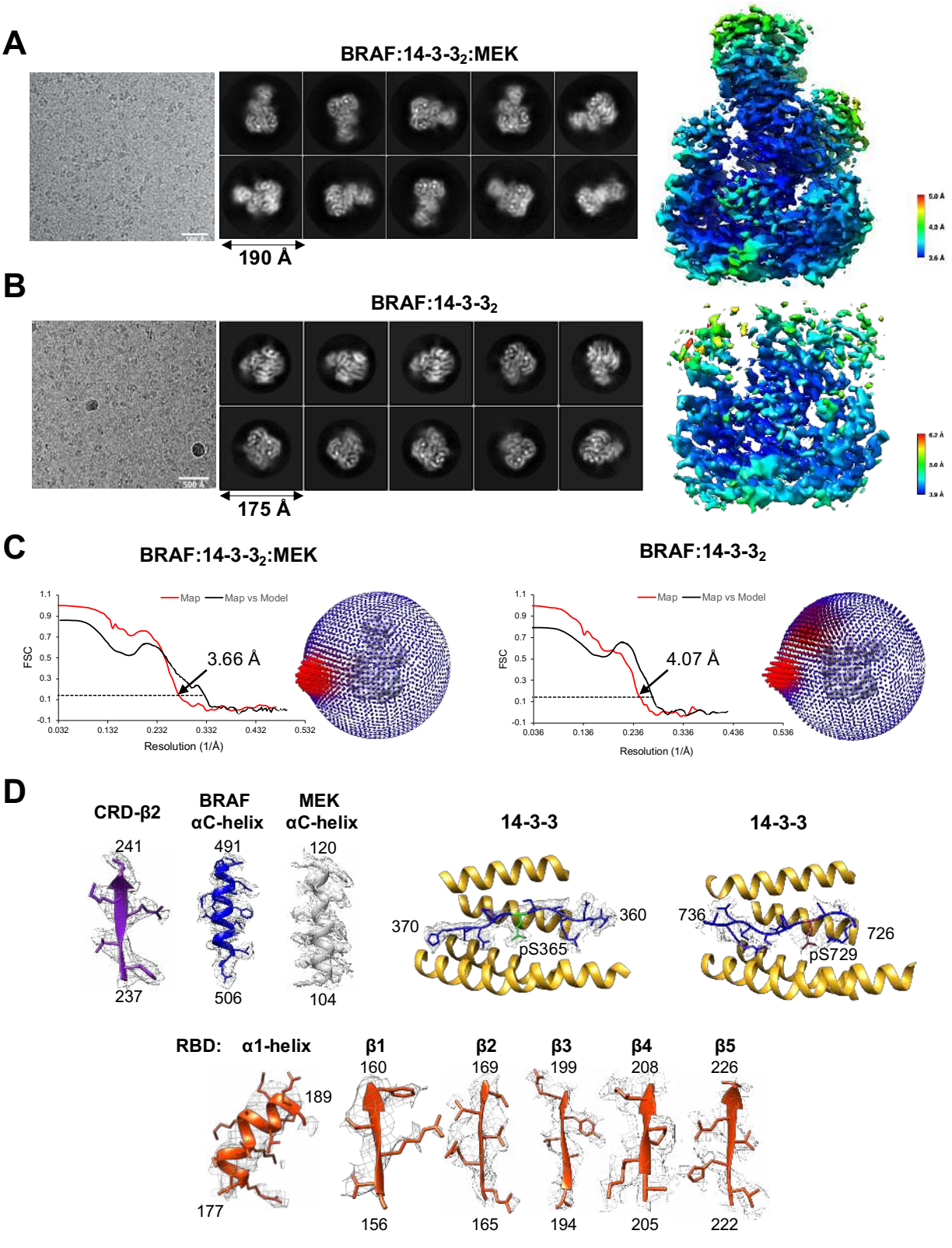
A
BRAF:14-3-3$_2$:MEK
190 Å
B
BRAF:14-3-3$_2$
175 Å
C
BRAF:14-3-3$_2$:MEK
Map
Map vs Model
FSC
3.66 Å
Resolution (1/Å)
BRAF:14-3-3$_2$
4.07 Å
D
CRD-β2
241
237
BRAF αC-helix
491
506
MEK αC-helix
120
104
14-3-3
370
360
pS365
14-3-3
736
726
pS729
RBD:
α1-helix
189
177
β1
160
156
β2
169
165
β3
199
194
β4
208
205
β5
226
222

Figure S4

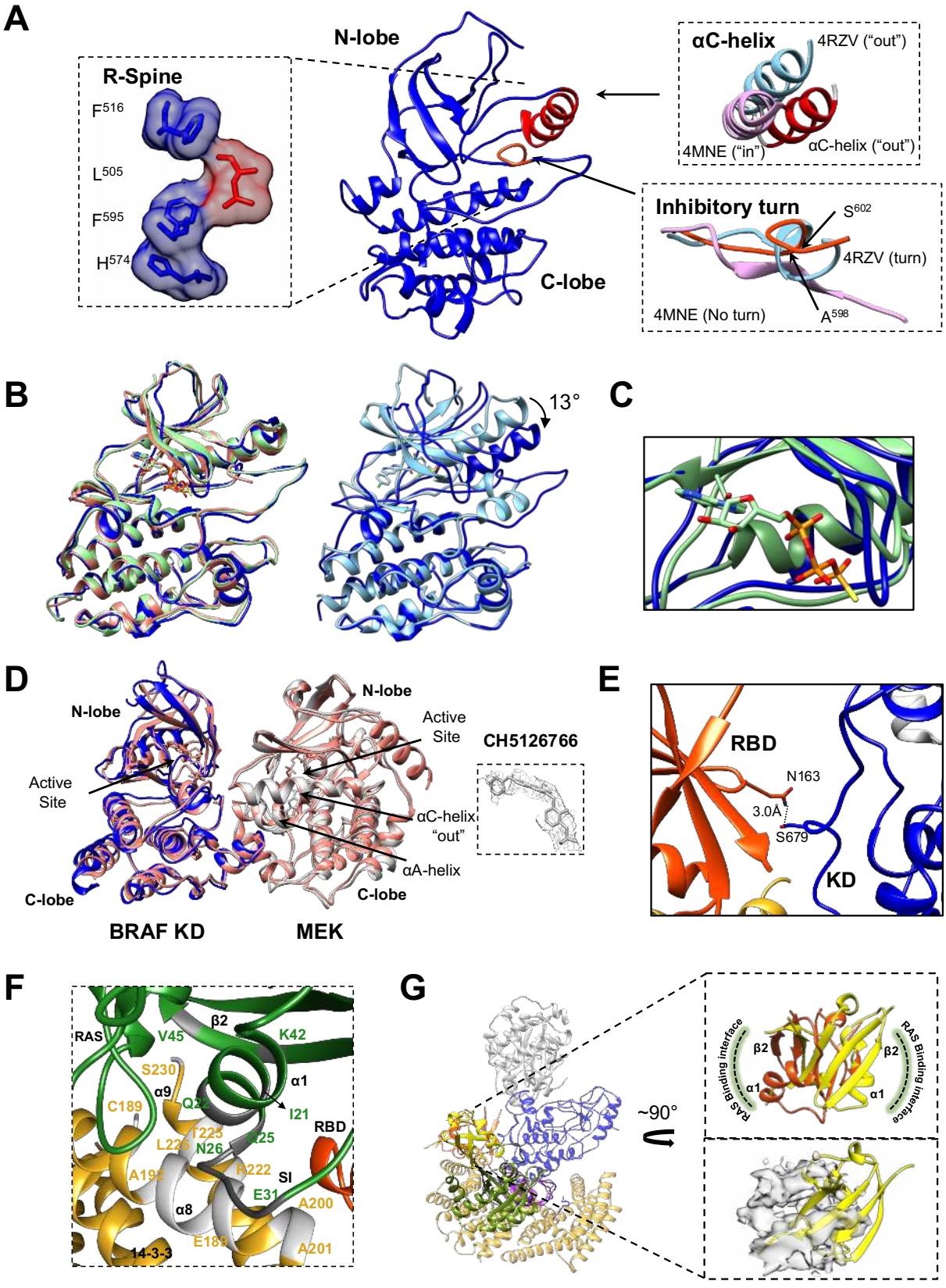
A
N-lobe
R-Spine
F516
L505
F595
H574
C-lobe
αC-helix
4RZV ("out")
4MNE ("in")
αC-helix ("out")
Inhibitory turn
S602
4RZV (turn)
4MNE (No turn)
A598
B
13°
C
D
N-lobe
Active Site
CH5126766
αC-helix "out"
αA-helix
C-lobe
BRAF KD
MEK
E
RBD
N163
3.0Å
S679
KD
F
RAS
V45
β2
K42
S230
α9
α1
C189
Q22
I21
RBD
T225
L226
N26
Q25
A192
R222
SI
E31
A200
α8
E189
A201
14-3-3
G
~90°
RAS Binding interface
β2
α1

Supplemental Figure Legends

Figure S1, related to Figure 1 and 2. Isolation and Characterization of Mammalian BRAF Complexes

Gel filtration (GF) profile (left) and SDS-PAGE analysis (right) for BRAF:14-3-3_2 (A), BRAF:14-3-3_2:MEK (B), and $BRAF_2$:14-3-3_2 (C) complexes. The arrows indicate the sample fractions used for cryo-EM studies. (D) Mass spectrometry analysis of the complexes isolated in A-C.

Figure S2, related to Figure 1. Cryo-EM Analysis of the $BRAF_2$:14-3-3_2 Dimer Complex

(A) Representative cryo-EM image and 2D class averages of $BRAF_2$:14-3-3_2 particles.

(B) $BRAF_2$:14-3-3_2 cryo-EM map colored according to local resolution.

(C) FSC curves of the cryo-EM density map (left). Reported resolutions were based on the FSC=0.143 criteria. Red curve is the $BRAF_2$:14-3-3_2 half map and black curve is the model versus map FSC. Euler angle distribution of particles used for the global reconstruction map (right).

(D) Cryo-EM densities corresponding to the αC-helix and the bound molecule of SB590885 in each KD protomer.

(E) Conformation of the KDs in the liganded $BRAF_2$:14-3-3_2 complex. The KD is shown in gray with the αC-helix (blue) in the active 'in' position and the R-spine residues (pink) aligned.

Figure S3, related to Figure 2. Cryo-EM Analysis of Autoinhibited BRAF:14-3-3_2:MEK and BRAF:14-3-3_2 Complexes

(A and B) Representative cryo-EM image and 2D class averages (left) and the cryo-EM map colored according to local resolution (right) of the BRAF:14-3-3_2:MEK (A) and BRAF:14-3-3_2 (B) complexes.

(C) FSC curves of the cryo-EM density map and euler angle distribution of particles used for the global reconstruction map of BRAF:14-3-3_2:MEK (left) and BRAF:14-3-3_2 (right). (D) Density maps of regions from BRAF (RBD, CRD, and KD), MEK, and 14-3-3 proteins.

Figure S4, related to Figures 2, 3 and 4. Structural Analysis of the Autoinhibited BRAF:14-3-3$_2$:MEK Complex

(A) The BRAF KD in the BRAF:14-3-3$_2$:MEK complex assumes the inactive conformation, with the αC-helix in the "out" position and the R-spine broken. Insets on the right show the comparison of specific regions of the present KD structure with published BRAF KD structures in the active (PDB ID 4MNE, in pink) and inactive (PDB ID: 4RZV, bound to the RAF inhibitor vemurafenib, in blue) conformations.

(B) Superimposition of the BRAF KD (blue) in the present structure with BRAF KDs of the previously reported cryo-EM BRAF(ATP-γS):14-3-3$_2$:MEK1 structure (with a Cα R.M.S.D. of 0.90 Å, PDB ID:6NYB, green), and the BRAF KD(AMP-PCP):MEK1 structure (with a Cα R.M.S.D. of 0.82 Å, PDB ID: 6U2G, salmon) (left), demonstrating the compact configuration of the N- and C-lobes in these inactive KD structures. Superimposition of the BRAF KD (blue) in the present structure with the vemurafenib-bound BRAF KD structure (with a Cα R.M.S.D. of 0.84 Å, PDB ID: 4RZV, light blue), which is an example of RAF inhibitor-bound BRAF KD structures exhibiting a more open N- and C-lobe configuration (right). Superimposition of these structures were done based on the C-lobe of the KD.

(C) Superimposition of the ATP binding pockets in the present BRAF:14-3-3$_2$:MEK structure (blue) and the previously reported cryo-EM BRAF:14-3-3$_2$:MEK1 structure bound to ATP-γS (PDB ID:6NYB, green).

(D) Superimposition of the BRAF KD:MEK component of the BRAF:14-3-3$_2$:MEK in the present structure (BRAF KD in blue and MEK in gray) with the previously reported crystal structure of the isolated BRAF KD:MEK1 dimer (PDB ID: 6U2G, pink) with a Cα R.M.S.D. of 0.97 Å.

(E) Potential interaction between N163 in the BRAF RBD (red orange) and S679 in the BRAF KD (blue).

(F) Potential steric clash at the RBD:14-3-3 interface between RAS residues I21-Q22 (α1-helix), Q25-E31 (SI region), K42 and V45 (β2 sheet) with 14-3-3 α8-helix residues C189, A192-E198, I200-A201 and α9-helix residues R222, L225-T226 and S230 upon superimposition of KRAS

onto the autoinhibited BRAF:14-3-3_2:MEK complex. RAS is colored in green, 14-3-3 in gold, and the potential clashing residues in RAS and 14-3-3 are colored in dark and light gray respectively.

(G) Rigid body superposition of the BRAF:14-3-3_2:MEK complex (colored as in Figure 2) and the KRAS:CRAF_RBD-CRD complexes (KRAS in green, CRAF RBD in yellow, and CRAF CRD in violet. PDB ID: 6XI7), with the alignment based on the CRD. Insets show the difference in the RBD orientation (top) and position (bottom) between the two structures. For the RBD position, the cryo-EM density map in the region of the BRAF RBD is shown in light gray and the CRAF RBD ribbon structure is in yellow.

Supplemental Tables

Table S1. Cryo-EM data collection, Refinement and Validation Statistics

	BRAF:14-3-3$_2$:MEK	**BRAF:14-3-3$_2$**	**BRAF$_2$:14-3-3$_2$**
Data Processing			
Data availability	PDB ID: 7MFD, EMB-23813	PDB ID: 7MFE, EMB-23814	PDB ID: 7MFF, EMB-23815
Magnification	130k, EFTEM mode	105k, EFTEM mode	105k, EFTEM mode
Voltage (kV)	300	300	300
Electron exposure ($e^-/Å^2$)	57	55	55
Exposure Rate ($e^-/Å^2/s$)	7.13	5.5	5.5
Dose/frame ($e^-/Å^2$)	1.14	1.10	1.10
Collection			
Number of frames collected per micrograph	50	50	50
Energy filter slit width	20eV	20eV	20eV
Defocus range (μm)	-0.8 to -2.5	-0.8 to -2.5	-0.8 to -2.5
Pixel size (Å)	1.058	1.348	1.348
Symmetry imposed	C1	C1	C1
Movies (no.)	3,976	5995	2,998
Initial particle images (no.)	1,824,538	2,496,302	2,159,824
Final particle images (no.)	142,852	198,731	203,343
Map resolution (Å)	3.66	4.07	3.89
FSC threshold	0.143		
Refinement			
Initial model used (PDB ID)	1FAR, 3WIG, 4FJ3, 4MNE, 5J17	1FAR, 4FJ3, 4MNE, 5J17	2FB8, 4FJ3
Map sharpening B factor ($Å^2$)	-100.5	-168.6	-167.4
Model composition			
Non-hydrogen atoms	9127	6843	8008
Protein residues	1147	859	1000
Ligands	1	0	2
Metals	2	2	0
B factors ($Å^2$)			
Protein	80.3	35.9	41.8
Ligand	94.6	42.2	23.6
r.m.s deviations			
Bond lengths (Å)	0.004	0.002	0.002
Bond angles (°)	0.659	0.570	0.522

Validation statistics			
MolProbity score	2.19	2.18	1.69
Clash Score	17.6	17.8	8.6
Rotamer outliers (%)	0	0	0.12
Ramachandran Plot			
Favored (%)	93.0	93.4	96.5
Allowed (%)	7.0	6.6	3.5
Outliers (%)	0	0	0
Model vs Data			
CC (mask)	0.61	0.64	0.71
CC (box)	0.68	0.63	0.69
CC (peaks)	0.53	0.50	0.61
CC (volume)	0.60	0.62	0.69
Mean CC for ligands	0.69	0.72	0.71

Table S2. Resource Table

REAGENT or RESOURCE	SOURCE	IDENTIFIER
Antibodies		
HaloTag mouse monoclonal	Promega	cat# G9211; RRID:AB_2688011
Rluc rabbit polyclonal	MBL International	cat# PM047; RRID:AB_1520866
GFP mouse monoclonal	Roche	cat# 11814460001; RRID:AB_390913
GFP rat monoclonal	MBL International	cat# D153-3; RRID:AB_591817
RAS10 mouse monoclonal	Millipore	cat# 05-516; RRID:AB_11211664
BRAF F-7 mouse monoclonal	Santa Cruz Biotechnology	cat# sc-5284; RRID:AB_626760
pS217/221-MEK rabbit polyclonal	Cell Signaling Technology	cat# 9121; RRID: AB_331648
MEK 1 mouse monoclonal	BD Biosciences	cat# 610122; RRID:AB_397528
MEK 2 mouse monoclonal	BD Biosciences	cat# 610236; RRID:AB_397631
Critical Commercial Assays		
Superose 6, 10/300 GL	Cytiva	cat# 29091596
Pierce Silver Stain Kit	Thermo Scientific	cat# 24612
NanoBRET Kit	Promega	cat# N1661
Halolink Resin	Promega	cat# G1915
Halo-TEV	Promega	cat# G6602
Deposited Data		
BRAF:14-3-3_2:MEK	This paper	Coordinates: PDBID: 7MFD Cryo-EM map: EMDB: EMD-23813
BRAF:14-3-3_2	This paper	Coordinates: PDBID: 7MFE Cryo-EM map: EMDB: EMD-23814
$BRAF_2$:14-3-3_2	This paper	Coordinates: PDBID: 7MFF Cryo-EM map: EMDB: EMD-23815
Coordinates of RAF-1 cysteine-rich domain	[45]	PDB ID: 1FAR
Coordinates of BRAF kinase domain bound to SB-590885	[48]	PDB ID: 2FB8
Coordinates of Human MEK1 kinase in complex with CH5126766 and MgAMP-PNP	[47]	PDB ID: 3WIG
Coordinates of 14-3-3 isoform zeta in complex	[49]	PDB ID: 4FJ3

with a diphoyphorylated CRAF peptide		
Coordinates of the BRAF:MEK1 complex	[46]	PDB ID: 4MNE
Coordinates of BRAF (R509H) kinase domain monomer bound to Vemurafenib	[32]	PDB ID: 4RZV
Coordinates of RAS Binding Domain (RBD) of BRAF	[44]	PDB ID: 5J17
Coordinates of BRAF-MEK1-14-3-3	[13]	PDB ID: 6NYB
Coordinates of BRAF:14-3-3 dimer complex	[23]	PDB ID: 6UAN
Coordinates of BRAF:MEK complex with AMP-PCP	[27]	PDB ID: 6U2G
Coordinates of BRAF dimer bound to 14-3-3	[24]	PDB ID: 6U2H
Coordinates of KRAS:CRAF_RBD-CRD complex	[37]	PDB ID: 6XI7
Coordinates of RAS:RBD-CRD	[39]	PDB ID: 7JHP
Experimental Models: Cell lines		
293FT (human)	ATCC	cat# PTA-5077, RRID:CVCL_6911
293T (human)	ATCC	cat# CRL-11268; RRID:CVCL_1926
HeLa (human, female)	ATCC	cat# CCL-2; RRID:CVCL_0030
Phoenix-Eco (human)	ATCC	cat# CRL-3214; RRID:CVCL_H717
NIH-3T3 (mouse)	ATCC	cat# CRL-1658; RRID:CVCL_0594
Recombinant DNA		
pCMV5-Halo-BRAF^{WT}	NCI-Ras Initiative	N/A
pCMV5-Venus-KRAS^{G12V}	NCI-Ras Initiative	N/A
pCMV5-Halo-KRAS^{G12V}	NCI-Ras Initiative	N/A
Lenti-puro-CMV-Ha-KRAS^{G12V}	NCI-Ras Initiative	N/A
pLHCX-BRAF^{FL}-RLuc8	[38]	N/A
pLHCX-BRAF^{FL} R158A-RLuc8	This paper	N/A
pLHCX-BRAF^{FL} R166A-RLuc8	This paper	N/A

pLHCX-BRAF^{FL} K183A-RLuc8	This paper	N/A
pLHCX-BRAF^{FL} R188L-RLuc8	This paper	N/A
pLHCX-BRAF^{FL} M186A/M187A-RLuc8	This paper	N/A
pLHCX-BRAF^{FL} M186W/M187W-RLuc8	This paper	N/A
pLHCX-BRAF^{FL} M186K/M187V-RLuc8	This paper	N/A
pCMV5-BRAF^{REG}-Halo	This paper	N/A
pCMV5- BRAF^{REG} M186A/M187A -Halo	This paper	N/A
pCMV5- BRAF^{REG} M186W/M187W -Halo	This paper	N/A
pCMV5- BRAF^{REG} M186K/M187V -Halo	This paper	N/A
pCMV5- BRAF^{REG} T241P -Halo	This paper	N/A
pCMV5-NanoLuc-CRAF^{Cat}	This paper	N/A
pCMV5-BRAF^{RBD}-Halo	This paper	N/A
pCMV5- BRAF^{RBD} M186A/M187A -Halo	This paper	N/A
pCMV5- BRAF^{RBD} M186W/M187W -Halo	This paper	N/A
pCMV5- BRAF^{RBD} M186K/M187V -Halo	This paper	N/A
pBABE-puro-Flag-BRAF	[38]	N/A
pBABE-puro-Flag-BRAF M186A/M187A	This paper	N/A
pBABE-puro-Flag-BRAF M186W/M187W	This paper	N/A
pBABE-puro-Flag-BRAF T241P	This paper	N/A
Software and Algorithms		
Serial EM	[40]	http://bio3d.colorado.edu/SerialEM
Relion 3.1	[41]	https://www3.mrc-lmb.cam.ac.uk/relion/index.php/Main_Page
MotionCor2	[42]	http://msg.ucsf.edu/em/software/motioncor2.html
Gctf	[43]	https://www2.mrc-lmb.cam.ac.uk/research/locally-developed-software/zhang-software/

COOT	[51]	https://www2.mrc-lmb.cam.ac.uk/personal/pemsley/coot
PHENIX	[52]	https://www.phenix-online.org
Chimera	[50]	https://www.cgl.ucsf.edu/chimera
Prism 8	N/A	https://www.graphpad.com/scientific-software/prism
Other		
R1.2/1.3 300 mesh Au holey carbon grids	Electron Microscopy Sciences	Cat# Q350AR1.3